J. Fluid Mech. (2004), *vol.* 507, *pp.* 143–174.
DOI: 10.1017/S0022112004008882 Printed in the United Kingdom

The oceanic boundary layer driven by wave breaking with stochastic variability. Part 1. Direct numerical simulations

By PETER P. SULLIVAN[1], JAMES C. McWILLIAMS[2] AND W. KENDALL MELVILLE[3]

[1]National Center for Atmospheric Research, Boulder, CO 80307, USA

[2]Department of Atmospheric and Oceanic Sciences and Institute of Geophysics and Planetary Physics, UCLA, Los Angeles, CA 90095, USA

[3]Scripps Institution of Oceanography, University of California, San Diego, La Jolla, CA 92093-0213, USA

(Received 1 August 2003 and in revised form 5 January 2004)

We devise a stochastic model for the effects of breaking waves and fit its distribution functions to laboratory and field data. This is used to represent the space–time structure of momentum and energy forcing of the oceanic boundary layer in turbulence-resolving simulations. The aptness of this breaker model is evaluated in a direct numerical simulation (DNS) of an otherwise quiescent fluid driven by an isolated breaking wave, and the results are in good agreement with laboratory measurements. The breaker model faithfully reproduces the bulk features of a breaking event: the mean kinetic energy decays at a rate approaching t^{-1}, and a long-lived vortex (eddy) is generated close to the water surface. The long lifetime of this vortex (more than 50 wave periods) makes it effective in energizing the surface region of oceanic boundary layers. Next, a comparison of several different DNS of idealized oceanic boundary layers driven by different surface forcing (i.e. constant current (as in Couette flow), constant stress, or a mixture of constant stress plus stochastic breakers) elucidates the importance of intermittent stress transmission to the underlying currents. A small amount of active breaking, about 1.6% of the total water surface area at any instant in time, significantly alters the instantaneous flow patterns as well as the ensemble statistics. Near the water surface a vigorous downwelling–upwelling pattern develops at the head and tail of each three-dimensional breaker. This enhances the vertical velocity variance and generates both negative- and positive-signed vertical momentum flux. Analysis of the mean velocity and scalar profiles shows that breaking effectively increases the surface roughness z_o by more than a factor of 30; for our simulations $z_o/\lambda \approx 0.04$ to 0.06, where λ is the wavelength of the breaking wave. Compared to a flow driven by a constant current, the extra mixing from breakers increases the mean eddy viscosity by more than a factor of 10 near the water surface. Breaking waves alter the usual balance of production and dissipation in the turbulent kinetic energy (TKE) budget; turbulent and pressure transports and breaker work are important sources and sinks in the budget. We also show that turbulent boundary layers driven by constant current and constant stress (i.e. with no breaking) differ in fundamental ways. The additional freedom provided by a constant-stress boundary condition permits finite velocity variances at the water surface, so that flows driven by constant stress mimic flows with weakly and statistically homogeneous breaking waves.

1. Introduction

Breaking waves at the sea surface promote vigorous mixing of momentum, energy, and scalars, and thus are a key process in upper-ocean dynamics and air–sea interaction. Wave breaking is dynamically important since it is believed to be the primary path for stress transfer between a wind-generated wave field and the underlying oceanic currents (Melville 1996). Observational evidence further shows that wave breaking leads to enhanced dissipation near the water surface and is, by introducing additional scales, the probable cause for departures from traditional scaling laws for rough-wall turbulent boundary layers (Cheung & Street 1988; Agrawal *et al.* 1992; Anis & Moum 1995; Terray *et al.* 1996; Gemmrich & Farmer 1999). Wave breaking frequently co-exists and interacts with Langmuir circulations that are generated by vortex forces associated with the wave Stokes drift (e.g. Thais & Magnaudet 1996; McWilliams, Sullivan & Moeng 1997; Zhou 1999; Kawamura 2000; Veron & Melville 2001). Wave breaking is triggered in the open ocean by wave–wave, wave–current, and wind–wave interactions (Melville 1996), but even in equilibrium conditions it is highly intermittent in space and time. For example, Melville & Matusov (2002) find that the percentage of surface area that is actively entraining air increases with wind speed cubed, and for wind speeds less than $15\,\mathrm{m\,s^{-1}}$ is at most $O(1\%)$. The whitecap coverage, which includes both active whitecaps and the residual foam after breaking has ceased, may be a factor of approximately 2 larger. Wu's (1988) compilation of whitecap measurements (see also Monahan & Woolf 1988) shows whitecap coverage less than 8% for wind speeds up to $20\,\mathrm{m\,s^{-1}}$. Wave breaking events occur over a spectrum of wavelengths ranging from centimetres or less ('micro-scale' breaking; Banner, Jones & Trinder 1989; Phillips & Banner 1974) to tens or hundreds of metres (plunging breakers in high seas; see review by Melville 1996) with the associated time scale of active breaking approximately proportional to the period of the breaking wave (Rapp & Melville 1990; Phillips, Posner & Hansen 2001; Melville & Matusov 2002). Thus, the momentum flux from breaking waves that drives oceanic currents occurs with a high degree of spatial intermittency over a broad range of scales and is locally much larger in magnitude than the mean wind stress at the surface of the ocean.

Scientists who model oceanic currents, however, typically do so using a mean surface wind stress, $\langle \boldsymbol{\tau} \rangle$, that varies smoothly in (x, y, t) on scales much greater than those of the wind gusts, oceanic turbulent eddies, and, of particular interest here, surface gravity-wave events that actually accomplish the stress transfer from winds to currents via waves and turbulent fluxes. High-frequency and small-scale motions generated by breaking waves are naturally filtered out by the grid resolution of large-scale oceanic models (e.g. McWilliams 1996; Large, McWilliams & Doney 1995), but even turbulence-resolving large-eddy simulation (LES) models of the oceanic boundary layer (OBL) (Skyllingstad & Denbo 1995; McWilliams *et al.* 1993, 1997; McWilliams & Sullivan 2001) typically ignore the intermittency of the surface stress. Direct numerical simulations (DNS) of breaking (Chen *et al.* 1999) are a notable exception, but they are at present limited in their space–time span to a single, two-dimensional event. Large-wave simulations (LWS) that attempt to resolve the large-scale wave evolution with a subgrid-scale model (e.g. Dimas & Fialkowski 2000) potentially could examine the impact of breaking waves on the OBL but require significant further development before fully coupled wave/boundary-layer calculations are possible. Recent advances with second-order turbulence closure models for oceanic boundary layers (e.g. Craig & Banner 1994; Craig 1996; Stacey 1999; Ly &

Garwood 2000; Burchard 2001) incorporate some wave breaking influences through parameterization with a surface source of turbulent kinetic energy and an empirically based surface roughness; however, these models ignore the momentum flux and energy intermittency of wave breaking that we view as essential ingredients.

We are interested in investigating what is missed in the resulting boundary layers by imposing the usual severe filtering on the stress-transmission process. Rather than assume the considerable burdens of a full microphysical simulation of air and water, however, we will follow a more modest approach of intermediate complexity. We go beyond the conventional forcing of a LES for the OBL that uses a $\langle \boldsymbol{\tau} \rangle$ which is uniform in (x, y) and varies in t only on atmospheric synoptic scales. This traditional stress is applied as a boundary condition at mean sea level, $z = 0$, and the model's resolved and parameterized (i.e. subgrid-scale) turbulent dynamics are relied upon to transport its effects into the interior. One important step towards including wave effects was previously taken using the wave-averaged theory that adds vortex forces and tracer advection terms proportional to the Stokes drift (Craik & Leibovich 1976; McWilliams & Restrepo 1999; McWilliams, Restrepo & Lane 2003), and its solutions in a LES model show important effects in the boundary layer turbulence, especially associated with the emergence of Langmuir circulations (Skyllingstad & Denbo 1995; McWilliams *et al.* 1997).

The further generalization we propose is the addition of three-dimensional random acceleration field, $\boldsymbol{A}(\boldsymbol{x}, t)$, for the resolved-scale momentum equation and a random work density, $W(\boldsymbol{x}, t)$, for the subgrid-scale turbulent kinetic energy equation, both of which are largest in the neighbourhood of $z = 0$ and decay with depth. These quantities represent the stress and energy transfer from breaking waves to OBL currents and turbulence. The spatial and temporal averages of $\boldsymbol{A}$ and W are non-zero. The distributions of $\boldsymbol{A}$ and W are chosen to match those measured for surface gravity waves, but their realizations will be as a stochastic simulation rather than an actual reconstruction from complete wave field measurements or a wave-dynamical calculation. Furthermore, the partition between $\boldsymbol{A}$ and W is a function of the LES model's grid resolution and the associated decomposition of the wave-breaking population, such that increasing resolution increases $\langle \boldsymbol{A}^2 \rangle$ and decreases $\langle W \rangle$, but preserves the total energy and momentum inputs from the wave breaking. The purpose of this paper is to specify this formalism for the stochastic forcing fields and to determine them consistently with field and laboratory observations of breaking waves (Rapp & Melville 1990; Melville & Matusov 2002; Melville, Veron & White 2002). To sequentially test the different components of our wave-breaking model, we only show idealized direct numerical simulation (DNS) solutions with the resolved acceleration field, $\boldsymbol{A}(\boldsymbol{x}, t)$ (§ 2), deferring to future reports a more complete LES formulation of surface wave effects that include the random work density $W(\boldsymbol{x}, t)$.

By introducing stochastic forcing terms into the otherwise deterministic PDE system of a turbulence-resolving model, we are adding a form of what the turbulence modelling community has called *stochastic backscatter*. Previously, this has only rarely been done. Its purpose, as ours here, is to model the effects of variability of smaller scale motions on the evolution of larger scales without calculating fully the smaller scale motions with a fluid dynamical model. Examples of this approach represent the effects of all turbulent motions on a two-dimensional shear layer (Leith 1990) and the effects of small-scale eddies in a three-dimensional inertial subrange (Chasnov 1987), with a particular application of the latter to the atmospheric planetary boundary layer over a flat surface (Mason & Thomson 1992; Schumann 1995). Our physical

context is different so our particular representation of stochastic backscatter is also. In particular we consider breaking waves as coherently structured events, and our forcing functions are based on this structure, although the time and location of breaking events are randomly distributed. Thus, our wave-breaking events are similar to coherent structures in flat-wall boundary layers (e.g. hairpin vortices and near-wall streaks: Robinson 1991; Adrian, Meinhart & Tomkins 2000) since they have finite lifetimes, interact nonlinearly with the background turbulence, and carry significant amounts of momentum and energy.

2. Formalism

The DNS model formulation is based on the incompressible Navier–Stokes equations with a linearized free surface condition approximated as a rigid lid at $z=0$ and a stochastic force, $\boldsymbol{A}$, that represents the primary effects of breaking on the boundary-layer currents:

$$\frac{\partial \boldsymbol{u}}{\partial t} = -(\boldsymbol{u}\cdot\nabla)\boldsymbol{u} - \frac{1}{\rho}\nabla p + \nu\nabla^2\boldsymbol{u} + \boldsymbol{A}. \tag{2.1}$$

Here $\boldsymbol{u}$ is the velocity vector; p is the pressure; and the fluid has uniform density ρ and viscosity ν. $\boldsymbol{A}$ is the new force to be modelled that contains the impulses (or accelerations) caused by a field of randomly distributed breakers. We intentionally omit other wave influences, in particular the contribution from Stokes drift (McWilliams *et al.* 1997), in this system of equations so as to isolate the effects of breaking waves.

2.1. *Representation*

Because of incompressibility, $\boldsymbol{u}$ is non-divergent, and so is its time derivative. Should we therefore choose $\boldsymbol{A}$ to be non-divergent? This is not mathematically necessary since the pressure force can mediate between a divergent $\boldsymbol{A}$ and a non-divergent $\partial\boldsymbol{u}/\partial t$. Nevertheless, since the net force induced on the currents by a breaking event must be non-divergent, it would be representationally more efficient to require this property for $\boldsymbol{A}$ (allowing e.g. a concise representation in terms of two scalar potentials in a Helmholtz decomposition). However, our present physical understanding is that a breaking wave provides a locally forward and downward impulse to the fluid, but the associated pressure field has not yet been measured well. The former effect can easily be represented in $\boldsymbol{A}$ (§ 3), but our ignorance of the p distribution leads us to abandon the non-divergence constraint at this stage of the research.

We define a local coordinate system, (ξ, η, z) with $\hat{\boldsymbol{\xi}}$ in the horizontal direction of the breaking (i.e. longitudinal), $\hat{\boldsymbol{\eta}}$ horizontally normal to it (i.e. transverse), and $\hat{\mathbf{z}}$ vertically upward. Then the depth-integrated acceleration in the breaking direction is

$$\frac{\partial}{\partial t}\int_{-H}^{0} \boldsymbol{u}\cdot\hat{\boldsymbol{\xi}}\,\mathrm{d}z' = \cdots + \int_{-H}^{0} A_\xi\,\mathrm{d}z', \tag{2.2}$$

where we assume that the breaking impulse vanishes at some depth above $z=-H$. We can compare this with the analogous relation with an imposed local surface stress, namely

$$\frac{\partial}{\partial t}\int_{-H}^{0} \boldsymbol{u}\cdot\hat{\boldsymbol{\xi}}\,\mathrm{d}z' = \cdots + \frac{1}{\rho^o}\hat{\boldsymbol{\xi}}\cdot\boldsymbol{\tau}^s, \tag{2.3}$$

and thus see that the horizontal component of $\boldsymbol{A}$ is a body force whose integrated magnitude replaces the more commonly used surface stress,

$$\int_{-H}^{0} \boldsymbol{A}_h \, \mathrm{d}z' = \frac{1}{\rho^o} \boldsymbol{\tau}^s,$$

where the subscript h denotes the horizontal vector component. We will assume that no horizontal acceleration occurs due to breaking in the $\hat{\boldsymbol{\eta}}$-direction, but there may be some in the $\hat{\mathbf{z}}$-direction (§ 3). In general, there will be some acceleration in the transverse direction as the breaker grows laterally; however, we believe that its neglect here is consistent with the other simplifications of the model.

In a field of breaking waves, this representation applies separately for each breaker. We relate the local coordinates for each breaking event to the global ones $(x,\ y,\ z)$ by a rotation ϕ and translation $(x_0,\ y_0)$ of the horizontal components:

$$\left.\begin{aligned} \xi &= (x - x_0)\cos[\phi] + (y - y_0)\sin[\phi], \\ \eta &= -(x - x_0)\sin[\phi] + (y - y_0)\cos[\phi]. \end{aligned}\right\} \tag{2.4}$$

For convenience we assume that $\hat{\boldsymbol{x}}$ is aligned with the mean breaking direction, i.e. $\langle \phi \rangle = 0$. Thus,

$$\boldsymbol{A} = (A_\xi \cos[\phi],\ \ A_\xi \sin[\phi],\ \ A_z) \tag{2.5}$$

in global coordinates.

$\boldsymbol{A}$ is a four-dimensional random field whose distribution is subject to the constraints above. We think of $\boldsymbol{A}$ as a sequence of wave-breaking events

$$\boldsymbol{A} = \sum_n \boldsymbol{A}^n, \tag{2.6}$$

where n is a discrete event index. For each event we represent $\boldsymbol{A}^n(\boldsymbol{x}, t)$ by a combination of random attributes with specified distribution functions and specified space–time shape functions. The list of random attributes of a breaking event is the following: surface location, (x^n, y^n); horizontal breaking direction, ϕ^n; onset time, t^n; duration, T^n; amplitude, A_o^n; longitudinal and transverse horizontal size, $L_\parallel^n$ and $L_\perp^n$; and vertical size, H^n. However, in applying these formulae for $\boldsymbol{A}$, we may find that it is sufficient to collapse the distributions for some of these attributes to their mean values. Associated non-dimensional shape functions for $\boldsymbol{A}$ represent the appropriate spatial structure and evolutionary sequence for a breaking wave. An exclusion principle can be applied to the random locations and onset times such that no two breaking events overlap in space and time.

From the superposition of breaking events, we can identify a constraint on integral stress transmission. The ensemble mean of (2.3) yields

$$\left\langle \int_{-H}^{0} \boldsymbol{A}_h \, \mathrm{d}z' \right\rangle = \frac{1}{\rho^o} \langle \boldsymbol{\tau}^s \rangle, \tag{2.7}$$

where the angle brackets represent both an average over (x, y, t) and over all breaking-wave events, that are assumed to be equivalent. In oceanic modelling the mean stress is usually estimated by a bulk formula,

$$\langle \boldsymbol{\tau} \rangle = \rho^a C_D |\boldsymbol{U}| \boldsymbol{U}, \tag{2.8}$$

where $\boldsymbol{U} = |\boldsymbol{U}| \hat{\boldsymbol{x}}$ is the mean near-surface wind and C_D is the drag coefficient, that depends on $\boldsymbol{U}$, the mean surface buoyancy flux, and the sea state, i.e. waves (Large & Pond 1982; Donelan 1998). In anticipation of the DNS in §§ 5 and 6, the

mean stress imposed at the top of the water in our simulations is determined by the flow Reynolds number, or ultimately by the feasible grid resolution.

3. Breaker model

The breaker model described here is based on the results of laboratory measurements of quasi-two-dimensional breaking by Rapp & Melville (1990), Loewen & Melville (1990), Melville *et al.* (2002) and related laboratory experiments reviewed in Melville (1996). It also draws on Phillips' (1985) statistical description of breaking and its implementation by Melville & Matusov (2002) who used airborne video imagery to measure the kinematics of breaking in the field. In the context of developing a breaking model, the primary results of the laboratory experiments are that the duration of active breaking is $O(T)$, the maximum fluid velocity during breaking is $O(c)$, and the depth of penetration of the broken fluid is $O(2a)$, where T, c, and a, are the characteristic period, linear phase speed, and amplitude, respectively, of the breaking wave. The laboratory experiments also showed that the post-breaking flow variables scaled with the pre-breaking variables even at large times. This suggests that Froude scaling of breaking, using the linear dispersion relationship, should be a good first approximation in a breaking model.

Phillips (1985) suggested, and Melville & Matusov (2002) showed, that breaking of sufficient strength to generate whitecaps in the field could be represented by statistics of the length of breaking fronts based on the speed of advance of the breaker. In the context of Froude scaling we expect this speed to be $O(c)$. The use of the linear wave speed to scale a strongly nonlinear process is partially justified by the fact that the phase speed of the Stokes limiting wave is only 11% greater than the corresponding linear phase speed. Thus we expect scaling based on the linear dispersion relationship to be a good first-order approximation; however, wave slopes are also important in relating wave amplitudes to wavelengths. In the open ocean Melville & Matusov (2002) found that over a spectrum of breaking events in the range $c = [1, 15]\,\mathrm{m\,s^{-1}}$ their measurements were consistent with Froude scaling of active whitecap coverage. Given this wide applicability of Froude scaling, the breaker field can then be built from a superposition of random events that individually obey the same scaling laws.

The modelling task is aimed at devising an appropriate prescription for a particular event $\boldsymbol{A}$ in § 2.1 (to clarify the presentation we omit the event index n in the following formulae).

For this first implementation, we collapse all the measured distribution functions for the breakers – except for time and location – to their mean values, and time and location are assumed to be uniform distributions except for an exclusion rule. We further assume that the wind and wave fields are aligned (i.e. $\phi = 0$ in (2.4)) and assume zero body force in the vertical direction. Hence (2.5) reduces to $\boldsymbol{A} = A_o(\hat{\boldsymbol{i}}, 0, 0)$. The time and space location of a particular event is randomly distributed, but once initiated the breaker life cycle is assumed known, i.e. A_o is a deterministic function of $(\boldsymbol{x}, t)$. Based on the observed properties of breaking waves in field measurements and laboratory studies (Rapp & Melville 1990; Melville & Matusov 2002; Melville *et al.* 2002), the following functional form for A_o is adopted:

$$A_o = k_b \frac{c}{T} \mathscr{T}(\alpha)\mathscr{X}(\beta)\mathscr{Y}(\delta)\mathscr{Z}(\gamma), \tag{3.1}$$

where $(\mathscr{T}, \mathscr{X}, \mathscr{Y}, \mathscr{Z})$ are space–time shape functions that describe the evolution of the event. We introduce the constant k_b to allow scaling of the breaker forcing relative

to the imposed stress τ_o (discussion in §§5 and 6). In our model, all breakers are assumed to be self-similar and separable in dimensionless time and space coordinates:

$$\alpha = (t - t_o)/T, \tag{3.2a}$$

$$\beta = (x - x_o)/c(t - t_o), \tag{3.2b}$$

$$\delta = 2(y - y_o)/\lambda, \tag{3.2c}$$

$$\gamma = z/\chi c(t - t_o), \tag{3.2d}$$

with $(t_o, x_o, y_o, z_o = 0)$ the onset time and position of the chosen breaker; (c, λ, T) are its phase speed, wavelength, and period. The wave characteristics (c, λ, T) are related to each other through the deep-water linear dispersion relation $c^2 = g\lambda/2\pi$ with $T = \lambda/c$. Notice that in the normalized vertical coordinate (3.2d) the constant $0 < \chi < 1$, which is just the aspect ratio of the depth to length of the breaker, controls the depth penetration of the breaker forcing.

The data available from laboratory and field measurements of breaking waves can guide the specification of $(\mathscr{T}, \mathscr{X}, \mathscr{Y}, \mathscr{Z})$, but are insufficient to pin down exact functional forms. Given this level of uncertainty we choose algebraic expressions that conform to the available data, but also satisfy practical computational constraints that they be smooth compact functions with continuous first derivatives. The algebraic forms used here are

$$\mathscr{T}(\alpha) = \mu_1\alpha^2[\exp(\mu_3(1-\alpha)^2) - 1], \quad 0 \leqslant \alpha \leqslant 1, \tag{3.3a}$$

$$\mathscr{X}(\beta) = \mu_2\beta^2(1-\beta)^2(1+\mu_4\beta^3), \quad 0 \leqslant \beta \leqslant 1, \tag{3.3b}$$

$$\mathscr{Y}(\delta) = (1-\delta^2)^2(1+\mu_5\delta^2), \quad -1 \leqslant \delta \leqslant 1, \tag{3.3c}$$

$$\mathscr{Z}(\gamma) = (1-\gamma^2)^2(1+\mu_6\gamma^2), \quad -1 \leqslant \gamma \leqslant 0, \tag{3.3d}$$

where the six constants μ_i remain to be specified. Two of the constants (μ_1, μ_2) are found from imposing the conditions $\int_0^1 \mathscr{T}(\alpha)\,\mathrm{d}\alpha = 1$ and $\max[\mathscr{X}] = 1$. The remaining μ_i-constants are picked to yield smooth functions; values of the constants used in the simulations are $\mu_i = [2.1, 5.1, 5, 10, 2, 2]$ along with $\chi = 0.2$. The resulting space–time shape functions are displayed in figure 1, and are observed to satisfy our design criteria.

4. Problem design

In order to cleanly evaluate our breaker model and isolate the impact of wave breaking on a turbulent shear flow we perform several direct numerical simulations of a generalized plane Couette flow. The model OBL flow is assumed to be a viscous, neutrally stratified, horizontally homogeneous turbulent flow confined between horizontal walls as sketched in figure 2. One aspect of breaking not included in the model is air entrainment. While small-scale ('microscale') breaking may not entrain dynamically significant quantities of air, this is not the case for larger active breakers for which Lamarre & Melville (1992) found that the work done against buoyancy forces in entraining air could account for up to 50% of the energy lost by the wave field during breaking. The inclusion of air entrainment and buoyancy effects is left to later developments of the model. In our coordinate system x is aligned with the main flow direction; y is the transverse direction; and z is measured upward from the lower boundary $z = -H$ to the water surface $z = 0$. The forcing near the upper boundary is variable: we specify constant current or a mixture of constant stress plus breakers. A passive scalar is also included in the problem to examine scalar

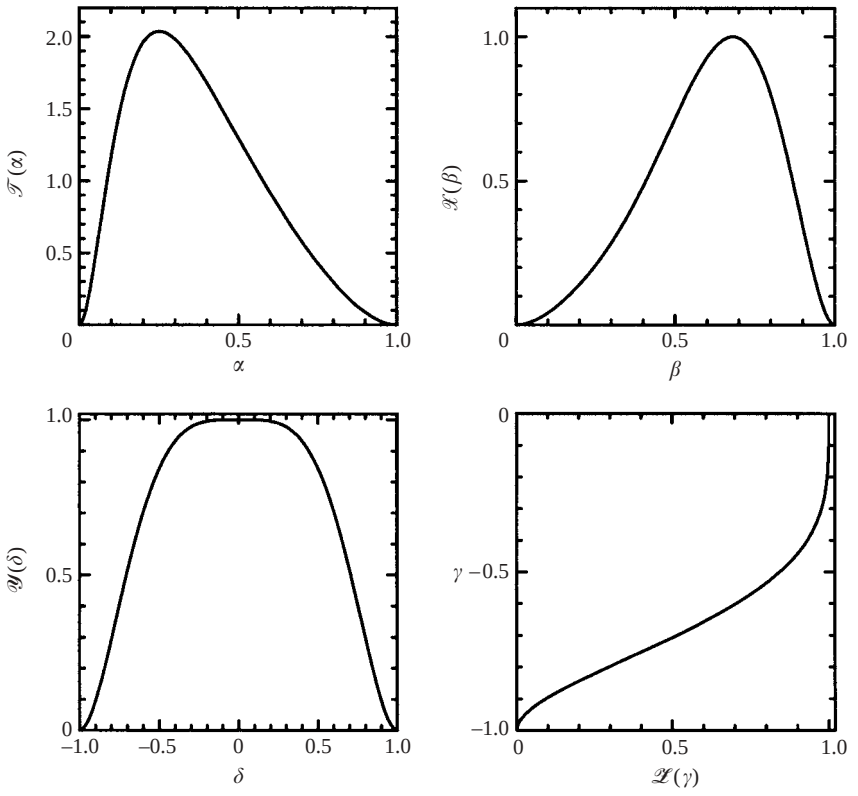

FIGURE 1. Non-dimensional space–time breaker shape functions $\mathscr{T}(\alpha)$, $\mathscr{X}(\beta)$, $\mathscr{Y}(\delta)$, $\mathscr{Z}(\gamma)$, which describe the breaker body force (see equation (3.1)).

transport. Figure 2 also depicts the orientation of a randomly located wave-breaking event at a particular instant in time. Active breaking occurs as time advances between $t_o \leqslant t \leqslant t_o + T$. During this time interval the breaker forcing expands downstream and deepens vertically while its extent in the transverse (y) direction remains constant. Outside the time interval of active breaking $A_o = 0$ for any particular event. The flow configuration in figure 2 is used to investigate the impact of breaking in two different flows: a quiescent fluid driven solely by a single breaking wave (§ 5) and fully turbulent wall layers in the presence of multiple random breakers (§ 6).

4.1. *Governing equations*

The governing equations for the flow depicted in figure 2 are the Navier–Stokes equations for a incompressible fluid written in non-dimensional form:

$$\frac{\partial \boldsymbol{u}}{\partial t} = -(\boldsymbol{u}\cdot\nabla)\boldsymbol{u} - \nabla p + \frac{1}{Re}\nabla^2\boldsymbol{u} + \sum_n A_o^n \hat{\boldsymbol{i}}, \tag{4.1a}$$

$$\frac{\partial \theta}{\partial t} = -(\boldsymbol{u}\cdot\nabla)\theta + \frac{1}{ScRe}\nabla^2\theta, \tag{4.1b}$$

$$0 = \nabla\cdot\boldsymbol{u}, \tag{4.1c}$$

Here the velocity vector $\boldsymbol{u} = (u\hat{\boldsymbol{i}}, v\hat{\boldsymbol{j}}, w\hat{\boldsymbol{k}})$; p is the pressure; A_o is the breaker impulse; and θ is an arbitrary scalar. In this set of equations, length and velocity scales (H, U_o) are used to make variables dimensionless. U_o is the fluid velocity at the upper boundary

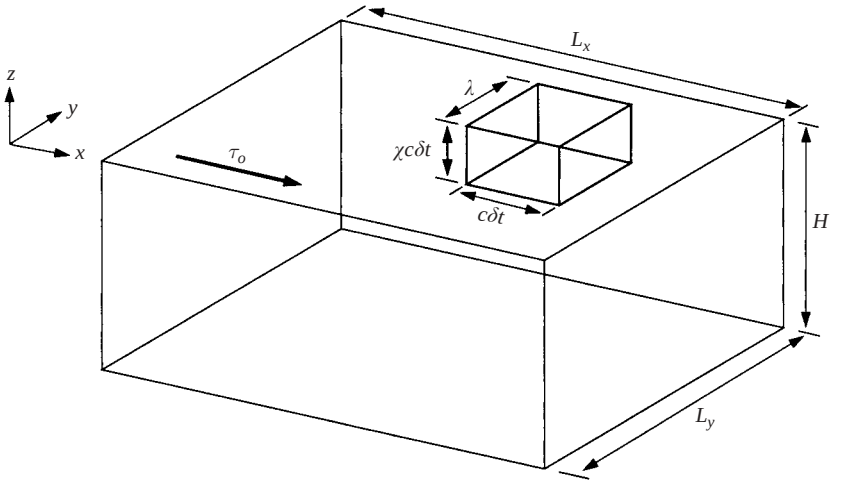

FIGURE 2. Sketch of the flow configuration illustrating a typical breaker and its orientation relative to the computational domain (L_x, L_y, H). (c, λ) are the breaker phase speed and wavelength. In the time window $t_o < t < t_o + T$, the breaker size is $(c\delta t, \lambda, \chi c\delta t)$ where $\delta t = t - t_o$, $\delta t \geqslant 0$. The vertical penetration of the breaker is determined by the parameter χ. Turbulent flows are simulated using a mix of τ_o and breakers A_o. To simulate classic Couette flow τ_o is replaced by a constant current U_o with $A_o = 0$.

in the Couette simulation (figure 2). The scalar is made dimensionless by the jump $\Delta\theta = \theta_l - \theta_u$ where (θ_u, θ_l) are constant values at $z = (0, -H)$, respectively. Then the dimensionless parameters governing the flow are the Reynolds number $Re = U_o H/\nu$ and Schmidt number $Sc = \nu/\upsilon$, where ν is the fluid viscosity and υ is the scalar diffusivity. For all calculations $Sc = 1$. (H, U_o) are also used to non-dimensionalize the properties of the imposed wave, i.e. when we refer to the phase speed of the wave c it is understood that it is non-dimensionalized by U_o.

4.2. *Numerical method*

The DNS code used to solve the continuity, momentum, and scalar transport equations (4.1) for flows with breakers is a variant of the wavy-surface simulation code fully described by Sullivan, McWilliams & Moeng (2000) and Sullivan & McWilliams (2002). The numerical method uses a co-located grid architecture for all variables instead of the staggered layout typical of most schemes. We use contravariant 'flux' velocities, Zang, Street & Koseff (1994), at the cell faces and employ the momentum-interpolation method of Rhie & Chow (1983) to maintain strong velocity–pressure coupling. The spatial differencing and time advancement in this DNS code are similar to those in the large-eddy simulation code described by Sullivan, McWilliams & Moeng (1996); pseudo-spectral differencing in (x, y)-planes and second-order finite differences in the z-direction are used and the time stepping is accomplished with a third-order explicit Runge–Kutta method using a fixed Courant–Friedrichs–Lewy (CFL) criterion. A non-uniform vertical z-mesh is used to resolve the top and bottom boundary layers; constant spacing is used in (x, y)-directions. For the present simulations a stationary rectangular computational mesh is used since the upper and lower boundaries are flat in physical space. Compared to simulations with time-dependent wavy lower boundaries, this simplifies the grid generation and increases the code efficiency. In particular, the pressure solver becomes exact, i.e. no iterations

are required at each time step to solve for the pressure since the variable coefficients in the pressure Poisson equation reduce to constants (Sullivan *et al.* 2000).

Mechanically, the inclusion of the breaker model requires special attention in the simulation code. As a simulation progresses, breaking events are introduced at random positions $(x_o, y_o, z=0)$ drawn from a uniform distribution, and tracking routines monitor their birth, growth, and death. Introduction of an explicit time-dependent forcing $A_o(\boldsymbol{x}, t)$ to the governing equations makes the system of equations non-autonomous. With our third-order Runge–Kutta time-stepping procedure, active breakers evolve at each sub-step, but new breakers are only allowed to be introduced at the end of a full time step. Meanwhile, an exclusion principle is applied so that as new events are added they are prevented from overlapping current existing breakers. We found an effective and simple means of controlling the white cap coverage, i.e. the total amount of surface water that is covered by all breaking waves, is to introduce breakers at a uniform rate throughout the course of the simulations. Potentially, the introduction of A_o can lead to a non-divergent velocity field. However, with the fractional step method used, the source term of the pressure Poisson equation includes all right-hand-side terms of the governing equations (including the breaker forcing), and a numerically divergence-free velocity field is obtained at each time step.

5. Isolated breaking event

Melville *et al.* (2002) describes a novel set of laboratory experiments that focus on the flow fields generated by an isolated nearly two-dimensional breaking wave. Digital particle image velocimetry is used to obtain two-dimensional (x, z) maps of the mean and turbulence velocity over the time history of a breaking event. This dataset provides an opportunity to test and evaluate elements of our breaking model.

5.1. *Computational details*

In order to mimic the Melville *et al.* (2002) laboratory experiments, the DNS code is configured to perform a rundown problem with a single breaker as the external forcing. The breaker space–time functions given in § 3 are used with the modification that the breaker is made two-dimensional in the simulations by setting $\mathscr{Y}(\delta)=1$. The DNS are performed in a computational domain of size $(L_x, L_y, H)/\lambda = (4, 2, 4)$ (figure 2). (100, 100) uniformly distributed gridpoints are employed in the horizontal directions with grid spacing $(\Delta x, \Delta y) = (0.04, 0.02)\lambda$. A non-uniform vertical mesh (96 total points) with grid clustering near the boundaries is employed. The spacing varies from $\Delta z = 0.015\lambda$ near the water surface to $\Delta z = 0.087\lambda$ at the domain centreline. Approximately 14 gridpoints are distributed in $z \in [-0.3, 0]\lambda$ and 31 gridpoints in $z \in [-1, 0]\lambda$. The computational domain and grid resolution are selected so that the mean fields produced by the breaker are well-resolved with a reasonable number of gridpoints and at the same time the domain is large enough such that the breaker can evolve freely without boundary interference. The time step is held fixed at $\Delta t = 0.094T$; this time step is much smaller than the time step determined from our usual CFL criterion. All simulations are advanced for more than 600 time steps or about 50 wave periods. The breaker phase speed (made dimensionless by U_o) is $c = 2.343$, and Reynolds number $Re = 8000$. They are selected to match the simulations in § 6. The Reynolds number based on (c, λ) equals 4700.

5.2. *Results*

The breaker forcing is primarily controlled by two constants: k_b, the breaker strength, and χ, the vertical depth penetration. In our simulations we varied these constants

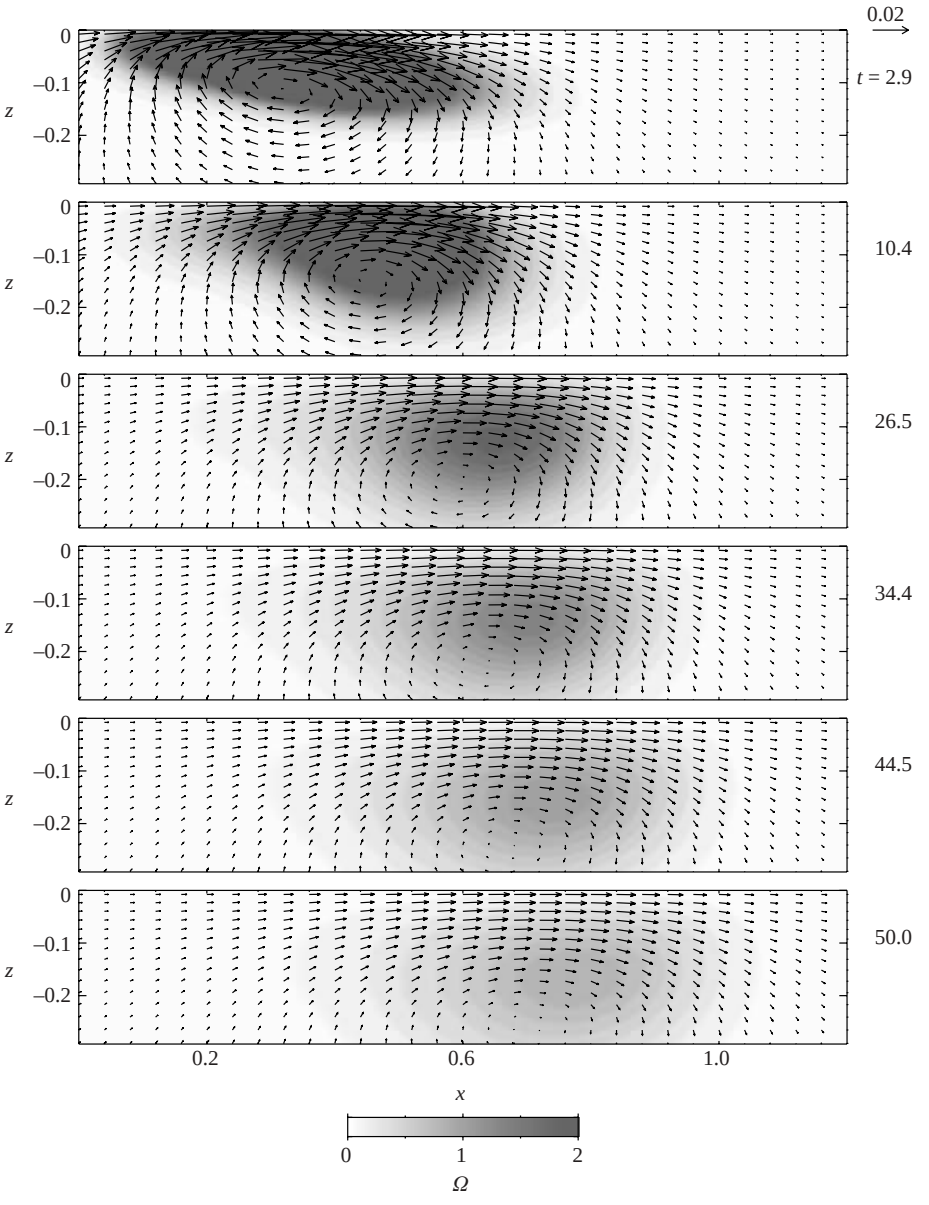

FIGURE 3. Mean two-dimensional velocity vectors $(u\hat{\boldsymbol{i}}, w\hat{\boldsymbol{k}})/c$ overlaying a shaded image of the vorticity field Ω_y at $t = [2.9, 10.4, 26.5, 34.4, 44.5, 50]$ from simulations of an idealized breaking wave.

over the range $0 < k_b < 0.36$, $0.1 < \chi < 0.2$. Over this parameter space, the breaker forcing varies smoothly (§ 3), and we find that the generated flow fields vary in a consistent manner. Typical flow patterns are displayed in figure 3 for a simulation with $(\chi, k_b) = (0.2, 0.18)$. The spatial and temporal variation of mean horizontal and vertical velocity vectors (u, w) are shown along with shaded contours of the transverse vorticity field $\Omega_y = \partial u/\partial z - \partial w/\partial x$. These are mean flow patterns obtained by averaging in the transverse (y) direction at fixed (x, z) locations. We emphasize that the time duration of the breaker forcing is short (one wave period), and thus the

results in figure 3 represent the long-time evolution of the breaker-induced flow fields. For comparison, comparable flow vectors from data described in Melville *et al.* (2002) are depicted in figure 4. The simulation results exhibit the formation of a vortex that propagates downstream and descends vertically after a breaking event. Based on the displacement of the vortex centre, we estimate that this vortex propagates with speed $8.7 \times 10^{-3}c$ that is in reasonable agreement with the measurement of $7.7 \times 10^{-3}c$ reported by Melville *et al.* (2002). The vortex in the simulations appears to descend slightly deeper compared to the measurements, but overall the mean flow vectors are comparable with the measurements. As expected, smaller values of χ reduce the descent of the vortex while larger values of k_b cause the vortex to propagate faster in x. We note that in laboratory measurements the strength of breaking (our k_b) is varied by controlling the slope of the wave packet. In the open ocean a wide spectrum of breaking waves are observed with varying strength (Melville & Matusov 2002).

In figure 5, values of the integrated mean flow kinetic energy are compared to measurements, where the integral is taken over the spatial domain shown in figure 3. Since the laboratory experiments are largely confined to the time after active breaking ($t > T$), a direct estimate of the strength of breaking parameter used here, k_b, cannot be made. The input to the experiments is a gain parameter that is proportional to the slope of the wave packet that focuses the breaking, but its direct relationship to the initial acceleration in the breaker, and hence k_b, is not well-established. Thus, for our comparison we use the mean kinetic energy at the non-dimensional time $t = 10$ to normalize both laboratory and simulation results. At long time, where we expect the simulations to be valid, the decay of the mean kinetic energy in the DNS and measurements are in good agreement; both decay at a rate approaching t^{-1} as predicted by Rapp & Melville (1990). At early time, the elevated values of kinetic energy in the laboratory data are a consequence of the orbital motion of surface waves that were still in the measuring region. Our model is not expected to reproduce this behaviour. Finally, we mention that the breaker strength, i.e. k_b, is expected to vary for two-dimensional and three-dimensional breakers. However, this variation has not been directly reported in measurements.

6. Multiple breakers with currents and turbulence

6.1. *Computational details*

A series of DNS with multiple breakers of varying strength imposed on a mixed layer with mean currents and turbulence is performed. The forcings near the top boundary are either constant current $\langle U_o \rangle$ at $z = 0$ (canonical Couette flow), constant horizontal stress $\langle \tau_o \rangle$ at $z = 0$, or any of three cases with a mixture of $\langle \tau_o \rangle$ and wave breaking $\sum_n A_o^n$. In the latter simulations, the integrated momentum forcing from the breaker field (to be compared with $\langle \tau_o \rangle$) is given by the volume-integrated breaker force(§ 2.1)

$$\langle B_f \rangle = \left\langle \int_{-H}^{0} \sum_n A_o \, \mathrm{d}z \right\rangle . \tag{6.1}$$

For discussion purposes, the simulations with a mixture of stress and breaker forcing are labelled with run names (table 1) that indicate the fractional amount of breaking. In table 1, run $\mathscr{B}$-000 is the simulation driven by constant stress and no breaking, while run $\mathscr{B}$-100 is at the opposite extreme, 100% breaking and no stress. The breaker forcing in the mixed runs $\mathscr{B}$-028 and $\mathscr{B}$-080 is 28% and 80% of the total forcing, respectively.

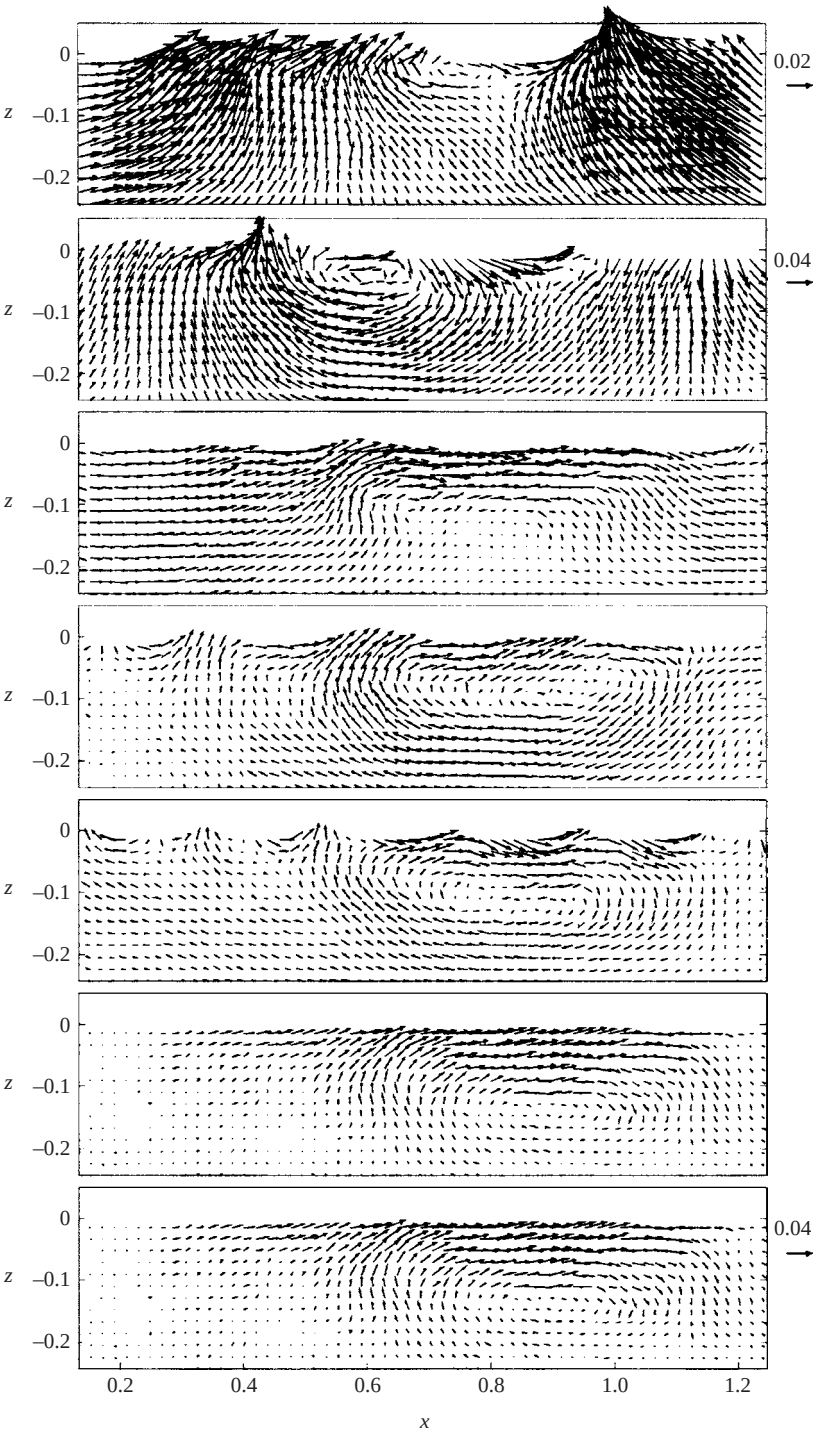

FIGURE 4. Ensemble-averaged two-dimensional velocity vectors $(u\hat{\boldsymbol{i}}, w\hat{\boldsymbol{k}})/c$ from laboratory measurements of an isolated breaking wave at times $t = [3, 10.5, 26.5, 34.5, 42.5, 50, 58]$ from Melville *et al.* (2002). Time increases from top to bottom in the panels. (z, x) are made dimensionless with the breaker wavelength. Based on the breaker scales, the Reynolds number of the flow $= 2.4 \times 10^6$.

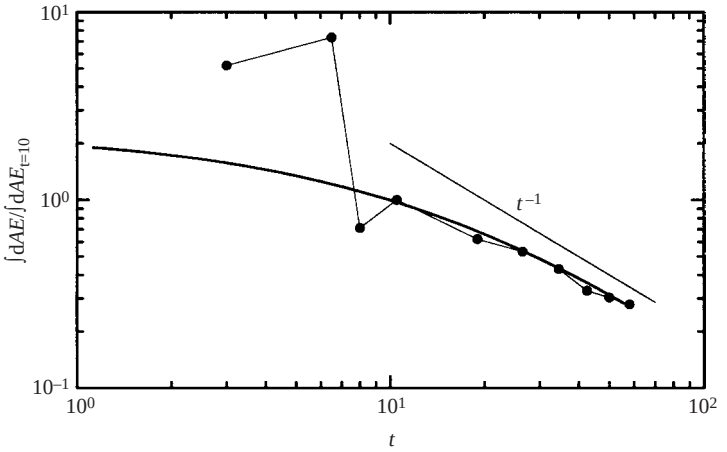

FIGURE 5. The integrated kinetic energy in the mean (u, w)-fields for an isolated breaker normalized by its value at time $t = 10$. Here $\int dAE = \int dA(u^2 + w^2)/2$ and the area of integration A is the domain $x/\lambda = [0, 1.2]$ and $z/\lambda = [-0.25, 0]$, i.e. the two-dimensional area shown in the panels of figure 3. Simulation results are indicated by a heavy solid line and the laboratory measurements from Melville *et al.* (2002) are denoted by dots and lines. At long time, results from the measurements and simulations decay with a slope approaching t^{-1} in agreement with the predictions by Rapp & Melville (1990).

Run name	k_b	$\langle B_f \rangle / u_*^2$	z_o^+	u_*	Symbol
Couette	0	0	0.13	0.030	○
$\mathscr{B}$-000	0	0	0.45	0.032	⊗
$\mathscr{B}$-028	0.23	0.28	0.65	0.033	✖
$\mathscr{B}$-080	0.70	0.80	2.60	0.034	◇
$\mathscr{B}$-100	0.93	1.05	4.24	0.034	●

TABLE 1. Simulation properties.

The design goal of the DNS with breakers is to vary the relative amounts of imposed stress at the top boundary $\langle \tau_o \rangle$ and average breaking force $\langle B_f \rangle$ while maintaining the same total stress at the bottom boundary $\langle \tau_b \rangle$ for all cases. This goal is only approximately achieved because of the long integration times required to gather statistics and the inherent unsteadiness caused by breaking; the latter effect leads to $\langle B_f \rangle / u_*^2 \approx 1.05$ for the case labelled $\mathscr{B}$-100 (§ 6.2). The friction velocity u_*, computed from the time and horizontal averages of the bottom stress ($u_*^2 = \langle \tau_b \rangle$), varies by 10% or less for the different runs (table 1). The strength of breaking (k_b) varies across the simulations, but the breaker phase speed, wavelength, and depth penetration are held constant; their dimensionless values are $(c, \lambda, \chi) = (2.343, 0.25, 0.2)$. Values of k_b in the simulations of table 1 are generally larger than the values used in the two-dimensional isolated-breaker run. Larger values are needed for simulations with three-dimensional breakers and a whitecap coverage constraint in order to match the stress of case $\mathscr{B}$-000.

Simulations with breaking also require a prescription for adding breakers as time advances. In the open ocean the rate of breaking ultimately depends in a complicated way on the history of the wind and wave fields. For the present simulations, we avoid

this complication and instead impose a rule that adds new breakers at a rate that maintains a realistic white cap coverage. By trial, we found that adding breakers at a rate of $R_b = 70$ events per unit of dimensionless simulation time is sufficient to generate a white cap coverage of about 1.6%, a value characteristic of the open ocean for winds less than $15\,\mathrm{m\,s^{-1}}$ (Wu 1988; Monahan & Woolf 1988). $R_b = 70$ is used in all simulations.

Simulations are performed in a computational domain of size $(L_x, L_y, H)/\lambda = (20, 12, 4)$ using $200 \times 200 \times 96$ gridpoints at a bulk Reynolds number $Re = U_o H/\nu = 8000$. At this Re and grid resolution, the turbulence is fully developed and well-resolved based on results from our prior DNS of flow over neutral and stratified water waves (Sullivan *et al.* 2000; Sullivan & McWilliams 2002; also see Komminaho, Lundbladh & Johansson 1996). Given the variation in u_* across the suite of runs, the wall Reynolds number $Re_* = u_* Re$ ranges from 240 to 272. The chosen domain size, number of gridpoints, and breaker properties represent a compromise between the competing requirements of computational cost, adequate resolution of the turbulence and breakers, and the desire to maintain a white cap coverage of $O(1\%)$. The horizontal spacing is $(\Delta x, \Delta y) = (0.1, 0.06)\lambda$ or in terms of wall units with a nominal $Re_* = 260$, $(\Delta x^+, \Delta y^+) = (\Delta x, \Delta y)Re_* = (6.5, 3.9)$. The variable vertical spacing is the same as that used for the isolated breaker simulations discussed in § 5.1. Δz^+ ranges from less than 0.5 at the boundaries to 5.46 at the channel centreline. These spacings satisfy the requirements for acceptable DNS resolution outlined by Moin & Mahesh (1998). At the end of active breaking, i.e. at $(t = t_o + T)$, the breaker impulse A_o for each event is represented by (10, 16, 11) gridpoints in (x, y, z).

All simulations are homogeneous in the lateral (x, y) directions (i.e. periodic boundary conditions) with no-slip (sticky) boundary conditions for all three velocity components at the lower wall. At $z = 0$, we set the vertical velocity $w = 0$ for all cases; in the Couette simulation the boundary conditions on the horizontal current components are $(u, v) = (U_o, 0)$; in the τ-driven flows the boundary conditions on the horizontal stress are $\boldsymbol{\tau} = (\tau_o, 0)$, and then (U_o, V_o) at the water surface are found as part of the solution. For the passive scalar, constant values are used at the upper and lower boundaries, $\theta = \theta_u$ and $\theta = \theta_l$ with positive jump $\Delta\theta = \theta_l - \theta_u$.

Initial conditions for the simulations are laminar profiles with low-amplitude random noise added near each boundary. The total number of computational steps varies from 75 000 to 115 000 time steps depending on the type of forcing. For all simulations the integration period is about 700 large-scale turnover times or 7000 wave periods. The flow is judged quasi-steady at about turnover time 180, and statistics are gathered starting from this point. Ensemble statistics, indicated by $\langle\ \rangle$, are obtained by a combination of temporal and spatial x, y averaging; the latter is indicated by $\langle\ \rangle_{xy}$. Velocity statistics, the current mean, variances, and momentum fluxes are normalized by u_* unless indicated otherwise. Scalar variables are normalized by the jump $\Delta\theta$. The deviation from a horizontal average (the turbulent part) is indicated by $(\ )'$, e.g. the x-component of the fluctuating horizontal current $u' = u - \langle u \rangle_{xy}$.

6.2. *Temporal development*

The temporal evolution of the flow fields illustrates important global impacts of breaking. We present results from simulation $\mathscr{B}$-100 since it represents the limiting situation of completely wave-generated currents. Figure 6 depicts the time history of several flow variables: the horizontally averaged current at the top of the water $\langle U_o \rangle_{xy}$, the volume-integrated breaker force $\langle B_f \rangle_{xy}$, the horizontally averaged bottom stress $\langle \tau_b \rangle_{xy}$, the number of active breaking events N_b, and the white cap coverage

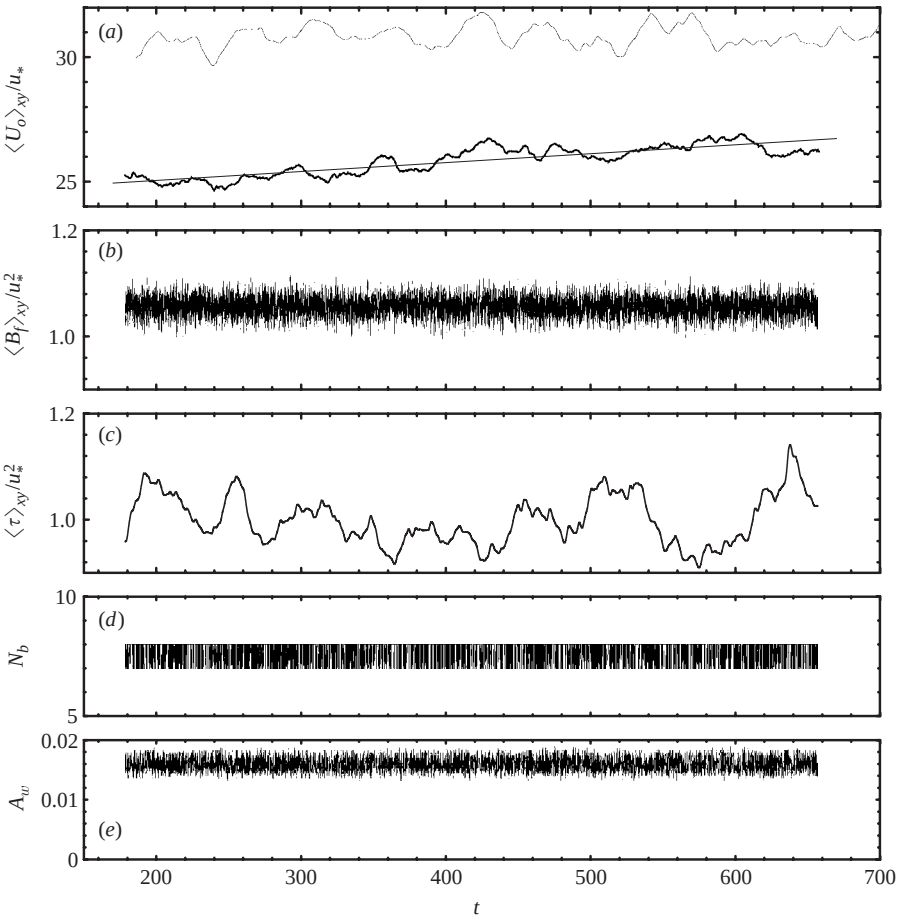

FIGURE 6. Temporal variation of selected parameters from case with 100% breakers ($\mathscr{B}$-100). (*a*) The horizontally averaged current at the top of the water $\langle U_o \rangle_{xy}/u_*$ ($\mathscr{B}$-100 thick line, case with zero breakers $\mathscr{B}$-000 thin line). The straight line is a linear regression to the results from $\mathscr{B}$-100. (*b*) The vertically integrated breaker force $\langle B_f \rangle_{xy}/u_*^2$. (*c*) The bottom stress $\langle \tau \rangle_{xy}/u_*^2$. (*d*) The number of active breaking events. (*e*) The fraction of horizontal surface area covered by active breaking events. Time is made dimensionless by U_o/h.

A_w. Notice that a field of intermittent breaking waves is capable of sustaining a mean current in the limit of zero wind stress (i.e. when $\langle \tau_o \rangle = 0$). The magnitude of the normalized current is, however, lower than its counterpart for flow driven by constant $\langle \tau_o \rangle$ alone. As we show later, the reduction in average current is a consequence of enhanced turbulence levels and resulting reduced mean gradients near the surface when breaking is present. Also the results with breaking show a small but clear trend for the mean current to increase with time. The breakers continuously supply momentum to the fluid irrespective of the current magnitude, and this momentum is not transported down to the bottom boundary at the same rate as in the no-breaker simulations (§ 6.5). Hence the mean current steadily increases and, in the presence of breaking, the generated flow fields are only statistically quasi-steady. This is a noticeable difference from flows driven by constant current or stress.

The variation of the volume-averaged breaker force illustrates that the forcing from breakers is larger than u_*^2 and concentrated at higher frequency than the slow

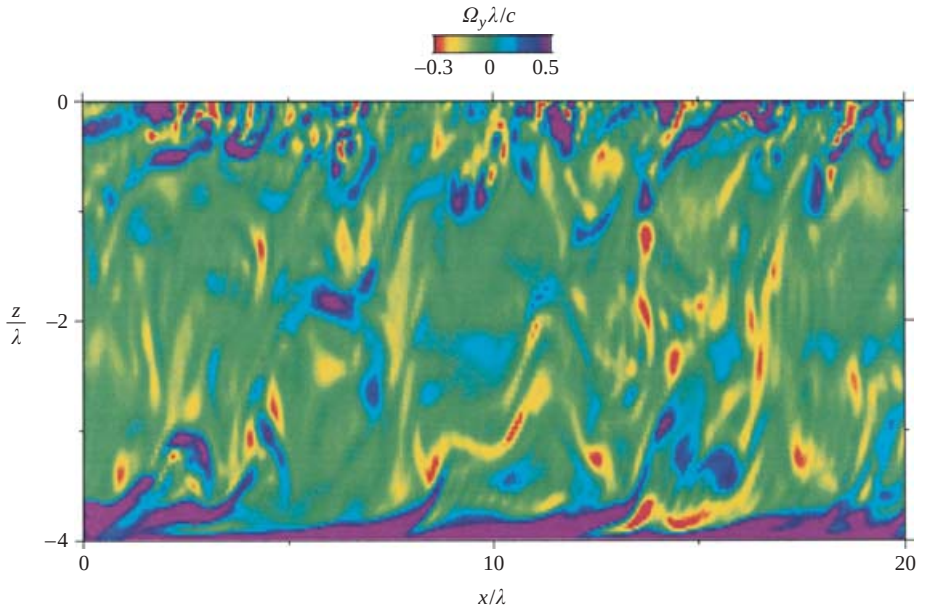

FIGURE 7. Snapshot of the instantaneous normalized vorticity field $\Omega_y\lambda/c$ in an (x,z)-plane for the case driven by 100% breaking. Note the contrast in the scale of vorticity near the water surface compared to the lower boundary.

oscillations in the bottom stress. The time scale of the imposed wave field c/u_* is of higher frequency than the dominant time scale of the turbulent field (with no breaking). As a result the breaker-induced velocities are also of high frequency. Computationally, this translates into longer simulation times since the allowable integration time step, which is inversely proportional to the maximum velocity, is reduced. The time step with 100% breaking is smaller by almost a factor of 2 compared to simulations with no breaking. We also notice that the average number of active events oscillates between 7 and 8 over the entire integration period. As a result, the white cap coverage is fairly constant with time. $A_w \approx 1.6\%$ results from the number of active events, the breaker spatial scale, and the lateral dimensions of the computational domain.

6.3. *Instantaneous flow structure*

The signature of breaking manifests itself in instantaneous snapshots of flow-field variables. In figures 7, 8, and 9 we present several two-dimensional cuts through the transverse vorticity (Ω_y), total current (u), vertical velocity (w), and vertical momentum flux ($u'w$) fields. The x,z vertical slice of Ω_y provides a vivid contrast in flow structures near the two boundaries. The presence of highly intermittent breaking induces small-scale, high-frequency vorticity near the water surface. As was noted previously in our simulation of an isolated breaker, a coherent pattern of Ω_y persists for multiple wave periods after active breaking ceases. Adrian *et al.* (2000) propose that the basic building blocks of turbulent wall flows are a synergistic interaction between low-speed streaks and hairpin vortices. The vorticity image shown in figure 7 provides some evidence that the usual process of turbulence generation in flat-wall boundary layers is disrupted by breaking. Near the lower boundary, large-scale patches of Ω_y contrast sharply with the small scales near the upper boundary. Animations

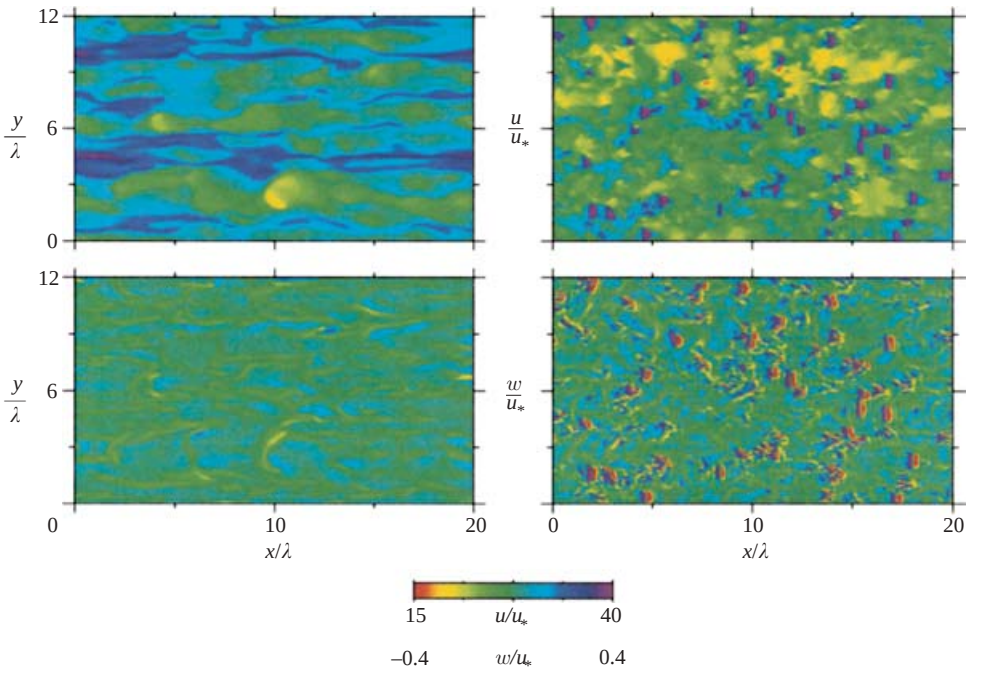

FIGURE 8. Snapshots of the instantaneous $(u/u_*, w/u_*)$ flow fields in (x, y)-planes very near the water surface at $z/\lambda = -0.0076$ for cases driven by constant stress (left panels) and with 100% breaking (right panels). At this depth $u'w/u_*^2$ is small and is not shown.

further show that the patterns in figure 7 near the upper and lower boundaries are a persistent feature of the flow and that breaking imposes its own time scale on the transverse vorticity generation process.

The images of the horizontal current, vertical velocity, and vertical momentum flux (figures 8 and 9) highlight the importance of breaking to the turbulence dynamics in the OBL surface layer. Very near the water surface, $z/\lambda = -0.0076$, the streamwise elongated streaky pattern characteristic of flat-wall boundary layers is modified by breaking; intermittent small-scale impulses are seen to dominate the horizontal currents. In figure 8 (upper right panel), we count numerous breakers, more than the 7 to 8 active breaking events noted in the time series of figure 6. This is evidence that the leftover debris from a breaker lives for an extended period, i.e. the temporal impact of a breaking wave is much longer than the active-breaker lifetime $T = \lambda/c$. The vertical velocity takes on a rich structure with an organized downwelling–upwelling pattern connected with each breaking event; downwelling occurs at the forward face and a return upwelling at the rear of each breaking event. Further, the intensity of the downwelling–upwelling events are significantly enhanced compared to the case with no breaking (compare figures 8 and 9). Vigorous impulses from the breaking waves at $z = -0.2\lambda$ impart strong vertical momentum flux, both negatively and positively signed, to the water column (see lower panels of figure 9); the momentum-flux-carrying structures are modified at depths below the penetration depth $z = -0.2\lambda$. From these images, we conclude that even though the observed white cap coverage of the breakers at the surface is very intermittent (less than 2% see figure 6) the presence of breaking eventually stirs the entire surface layer of the OBL.

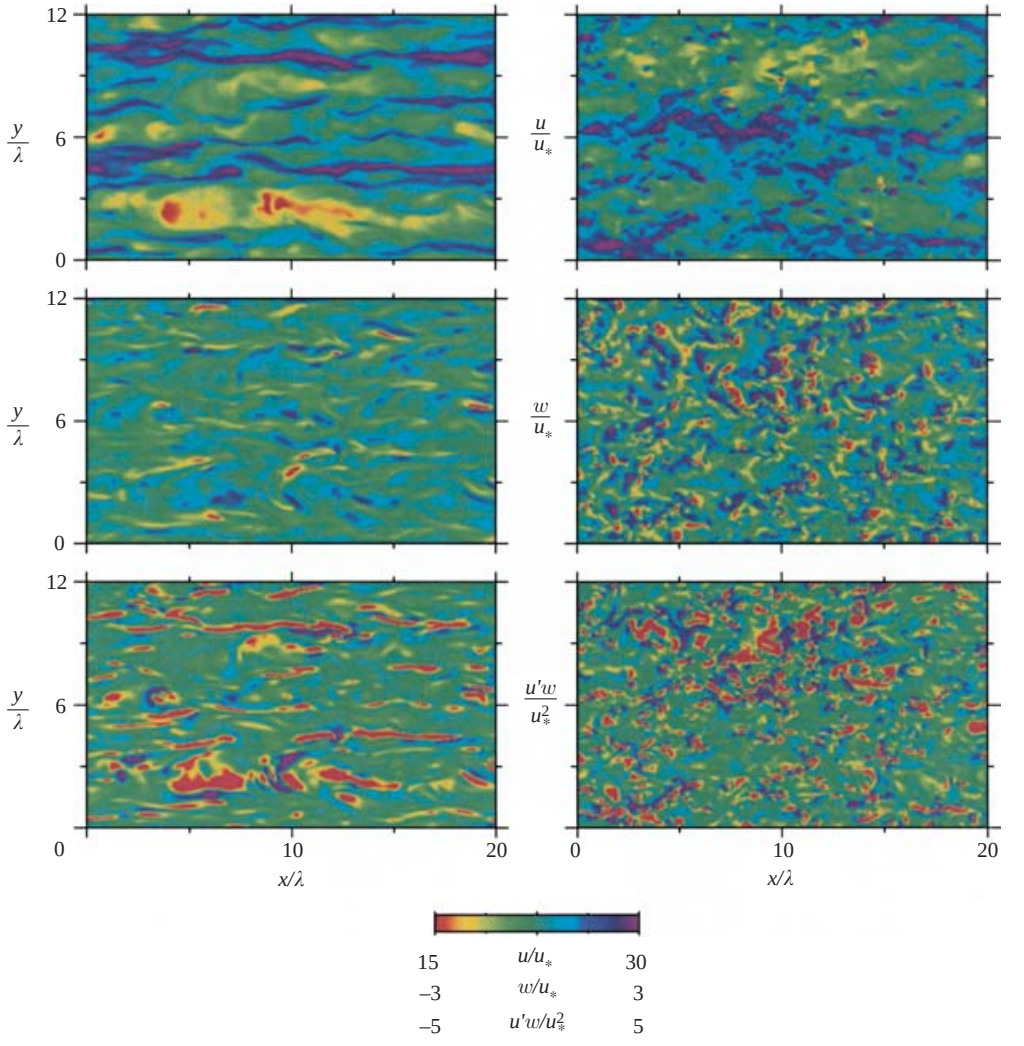

FIGURE 9. Snapshots of the instantaneous $(u/u_*, w/u_*, u'w/u_*^2)$ flow fields in (x, y)-planes at $z/\lambda = -0.2$ for cases driven by constant stress (left panels) and with 100% breaking (right panels).

6.4. *Mean profiles*

The upper surface boundary condition and the amount of wave breaking have an impact on the mean horizontal current and scalar distribution. This is illustrated in figure 10 where vertical profiles are displayed in the normalized global coordinates $(\langle u\rangle/\langle U_o\rangle, \langle\theta\rangle/\Delta\theta)$ versus z/λ for the five different simulations. The simulation of turbulent Couette flow provides a baseline to judge the influence of breakers. With sufficient averaging, the mean current and scalar profiles in this case are symmetric about the channel centreline, as required. Turbulent mixing weakens the mean profile vertical gradients in the mid-section of the channel while the no-slip boundaries generate sharp transitions near the upper and lower walls. The τ-driven flows display the same broad features as the Couette case, but the mean profiles are clearly asymmetrical about the mid-plane $z/\lambda = -2$ with the asymmetry increasing

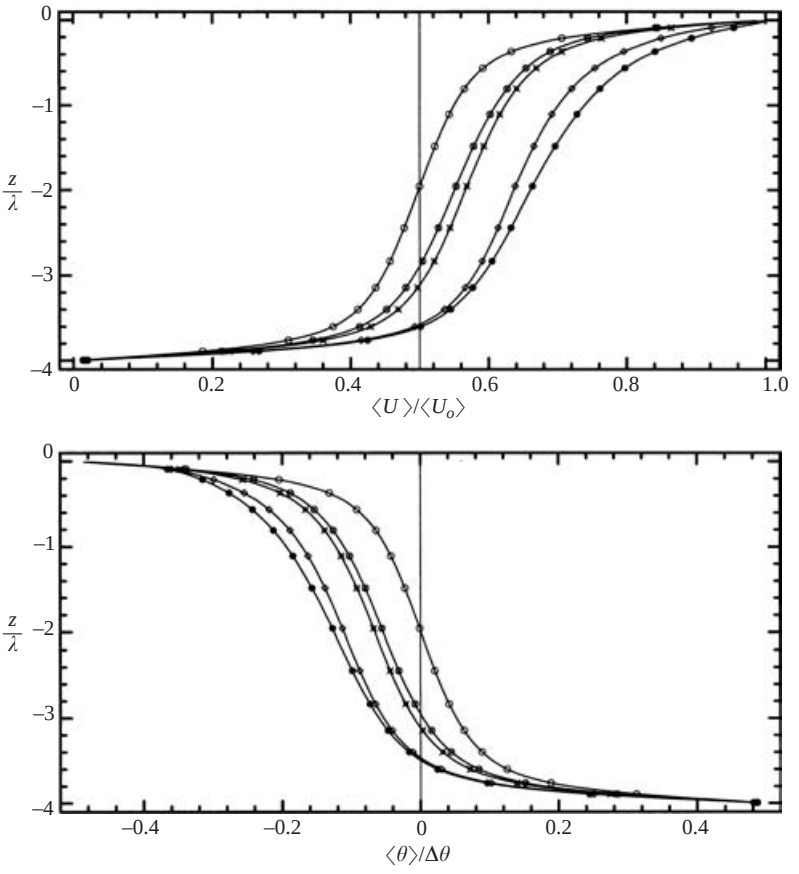

FIGURE 10. Vertical profiles of the mean velocity and scalar fields in global coordinates. The particular simulation (see table 1) is denoted by the symbol: ○, Couette; ⊗, $\mathscr{B}$-000; ⋆, $\mathscr{B}$-028; ◇, $\mathscr{B}$-080; ●, $\mathscr{B}$-100; and is used in all following figures.

as the external forcing shifts from constant stress to intermittent breaking. It is also important to notice that the profiles for the stress-driven flow with no breaking, case $\mathscr{B}$-000, are not equal to those of the Couette simulation, but fall closer to the results for the case with mild breaking $\mathscr{B}$-028. This difference between the Couette and $\mathscr{B}$-000 cases was initially unexpected but is a direct consequence of the form of the upper boundary condition, constant stress versus constant current. The extra freedom permitted by a constant-stress boundary condition allows the current to oscillate in time and space at the water surface. Thus the horizontal current fluctuations are finite at $z=0$; a strict no-slip condition on the horizontal velocity components requires $(u', v')=0$ (§6.5). Even in the absence of stress intermittency and other wave effects, the surface layer of an oceanic boundary layer differs from its atmospheric counterpart (over a rigid surface) in a fundamental way. The difference between constant-current and constant-stress driving for oceanic mixed layers is also briefly noted by (Zhou 1999, p. 166). Further examination of the profiles near the upper surface shows that the normalized vertical profile gradients decrease as the breaking increases, suggestive of an enhanced turbulence level.

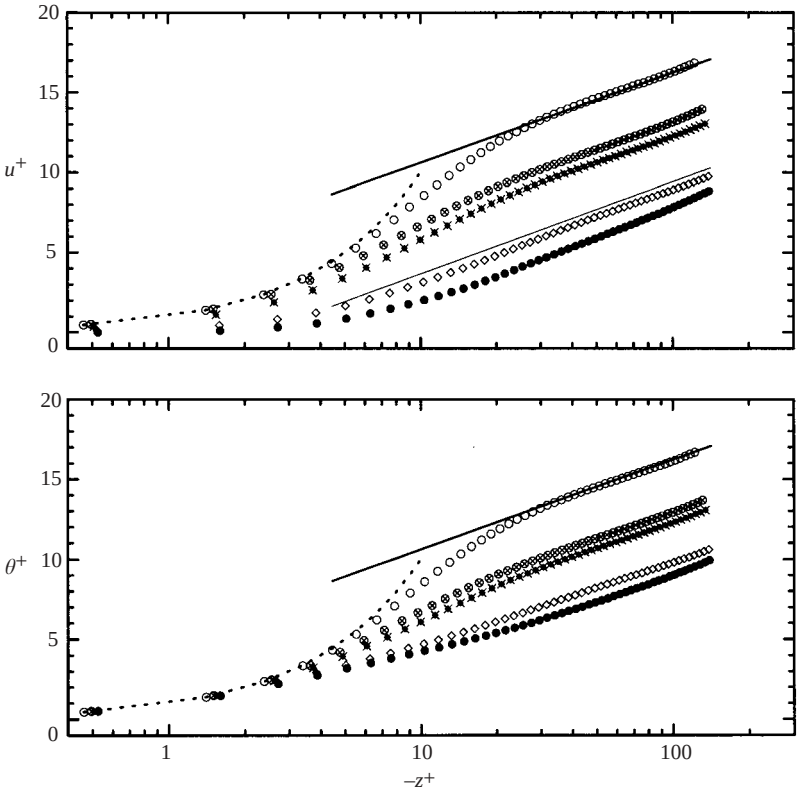

FIGURE 11. Vertical profiles of the mean velocity and scalar fields in wall coordinates. The dotted line is the linear curve $(u^+, \theta^+) = -z^+$; the thick solid line is the log-linear law $(u^+, \theta^+) = \ln(-z^+)/\kappa + b$ valid for smooth walls with $(\kappa, b) = (0.41, 5)$; and the thin solid line is the log-linear law for fully rough walls with $(\kappa, b) = (0.41, -2.1)$. The different simulations are: ○, Couette; ⊗, $\mathscr{B}$-000; ⋆, $\mathscr{B}$-028; ◇, $\mathscr{B}$-080; ●, $\mathscr{B}$-100.

To illustrate the changes induced by the breakers we display the current and scalar profiles in terms of traditional wall variables written in the defect form

$$u^+ = \frac{\langle U_o \rangle - \langle u \rangle}{u_*}, \quad \theta^+ = \frac{\theta_u - \langle \theta \rangle}{\theta_*}, \quad z^+ = \frac{z u_*}{\nu}, \tag{6.2}$$

where $\theta_* = -\langle \tau_\theta \rangle / u_*$ and $\tau_\theta = (ScRe)^{-1} \partial\theta/\partial z$ is the scalar flux at the bottom boundary. The most striking impression in figure 11 is the systematic downward shift in the horizontal current and scalar profiles with increasing k_b compared to the Couette simulation. From the perspective of classic wall-bounded shear flow, this downward shift in the current profile is equivalent to an increase in surface roughness z_o (e.g. Schlichting 1968, pp. 568–586; Cebeci & Bradshaw 1988, p. 167; Raupach, Antonia & Rajagopalan 1991; Leonardi *et al.* 2003). To quantify the increase in z_o, we fit the log-linear portion of the different profiles in figure 11 with the relation $u^+ = \ln(-z^+)/\kappa + b$, where $\kappa = 0.41$. The effective roughness $z_o^+ = z_o u_*/\nu = \mathrm{e}^{-\kappa b}$ varies from 0.13 to 4.24 for the different simulations (table 1). Thus, with strong wave breaking the effective roughness can be a factor of 30 times larger than for the case with a constant-current boundary condition. In figure 11, the velocity profile for a full rough wall layer (e.g. Schlichting 1968, pp. 584) is displayed; notice that the velocity profile from our

low-Re DNS with 100% breaking is thus effectively in the fully rough regime. The transition to a log-linear variation occurs at smaller z^+ values in the situation with strong wave breaking, a further indicator of an increase in z_o^+. Since we hold u_* approximately constant across the series of simulations, the enhanced vertical mixing from intermittent breaking is the source of the effective increase in surface roughness.

We note that our predictions of surface-roughness enhancement due to breaking waves is supported by the laboratory measurements of Cheung & Street (1988). In their wind-wave tank experiments, current profiles near the air–water interface are measured beneath growing and breaking waves generated by varying wind speed ($1.5\,\mathrm{m\,s^{-1}}$ to $13.1\,\mathrm{m\,s^{-1}}$). The authors do not quantify the amount of wave breaking but mention that the visual appearance of the water surface varied from smooth to rough for the range of wind speeds considered. Figure 1 of Cheung & Street (1988) shows a pronounced downward shift in the current profiles with increasing wind speed, with a full rough regime reached at higher wind speeds. Our DNS predictions are at least in qualitative agreement with these results. However, the authors also report a change in the slope of the current profile, i.e. a larger value of the von-Kármán constant (κ) at high wind speed. We do not find this even with 100% breaking, but speculate as they do that other wave influences are present in their experiments.

Finally, z_o is an unknown but critical parameter in second-order closure models of the oceanic mixed layer (e.g. Craig & Banner 1994; Craig 1996). In this type of model, the oceanic surface is assumed rougher with breaking waves, and a z_o-parameterization is used to tune the model predictions; values as large as one sixth (16%) of the breaker wavelength are used. In our DNS z_o is a computed output. Hence, the present results confirm an increase in z_o with breaking, but also highlight that changes in the oceanic surface layer are induced by the intermittency of breaking and additionally by the type of surface boundary condition. For our particular breaking waves, we find z_o/λ between 0.04 to 0.06 when breaking constitutes 80% to 100% of the total stress. This is lower than the values used in the second-order closure modelling of Craig & Banner (1994).

6.5. *Variance and momentum-flux profiles*

Because our breakers are spatially evolving three-dimensional structures, they are capable of generating three-dimensional turbulence fields. This is reflected in the (u, v, w)-variance and turbulent kinetic energy ($\mathrm{TKE} = \langle u_i u_i \rangle/2$) profiles shown in figure 12. Comparison of the profiles reveals that turbulence is mainly enhanced in the region $z/\lambda = -0.2$ to 0, with the vertical current (w^2) variance exhibiting the largest change; in case $\mathscr{B}$-100 at $z/\lambda = -0.2$, w^2 is about 8 times larger than its counterpart in the Couette simulation. The depth over which the breakers influence the w-variances also extends deeper, down to about 60% of λ. Enhanced levels of w-variance are a result of the vigorous downwelling–upwelling pattern associated with breaking events (figures 8 and 9). The measurements of vertical variance by Cheung & Street (1988) (see their figure 3) are in agreement with these predictions. Notice that significant increases are also observed in the transverse v-variances. Flow visualization of instantaneous v-currents shows that strong plus and minus signed v' is generated (by transverse pressure gradients) along the central x-axis of each breaker. As alluded to previously, the impact of the surface boundary condition on the magnitude and vertical distribution of variance is visible in figure 12. With a constant-stress boundary condition (case $\mathscr{B}$-000), the (u, v)-variances are finite at $z = 0$, and the extra mixing caused by this surface layer turbulence mimics, at least qualitatively, that of weak breaking waves. The increase in TKE, which is dominated

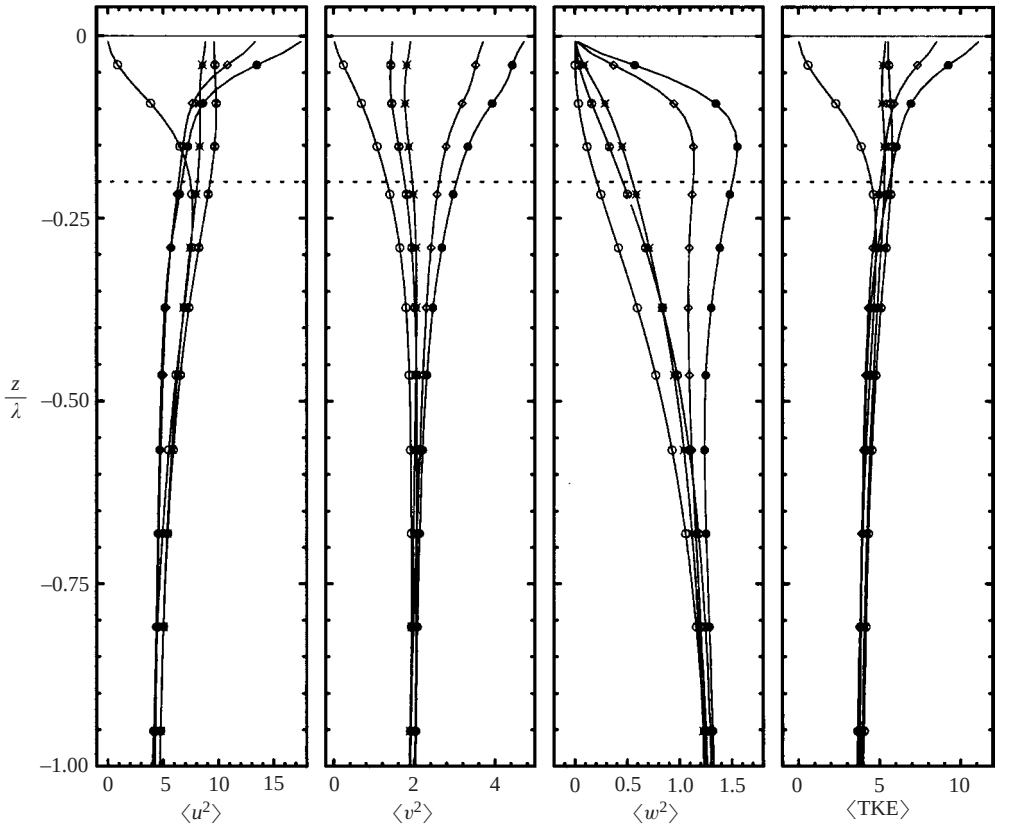

FIGURE 12. Vertical profiles of the (u, v, w)-variances and the turbulent kinetic energy (TKE) normalized by u_*^2 near the water surface. The (fixed) maximum breaker penetration depth is indicated by the dotted horizontal line. The different simulations are: ○, Couette; ⊗, $\mathscr{B}$-000; ⋆, $\mathscr{B}$-028; ◇, $\mathscr{B}$-080; ●, $\mathscr{B}$-100.

by the large u-variance, is confined to the near-surface breaking region. The impact of breaking on scalar variance, shown in figure 13, is less dramatic, and at $z/\lambda = -0.2$, θ'^2 with 100% breaking is actually smaller than the $\mathscr{B}$-000 case. This result can be interpreted in terms of the scalar variance budget: the high levels of breaker-induced turbulence weaken the mean scalar gradient $\mathrm{d}\langle\theta\rangle/\mathrm{d}z$ (figure 11) which in turn lowers the production of θ'^2.

The distribution of variance across scales for the (u, v, w, θ) variables at $z/\lambda = -0.2$ is illustrated by the power (energy) spectra shown in figure 14. Consistent with the total variances (figure 12), the spectral distribution of energy for v and w is most influenced by breaking. At a depth of $z/\lambda = -0.2$, we observe that the power increases significantly in the (v, w)-fields at all wavenumbers beyond $k_x > 10$ with strong breaking. The impact of the breaker forcing appears to be smeared out over a broad range of scales even though the dominant wavenumber of breaking in our simulations $k_{x,b} = 2\pi/\lambda \approx 25$. Because our simulations are not wave resolving, the computed spectra do not display a peak at the wave orbital frequency as observed in field measurements (e.g. Terray *et al.* 1996). There is also a hint that the power at low wavenumbers (large scales) in the (u, θ)-fields is reduced in the presence of strong breaking, more so for θ. This is also found in the total variances shown previously.

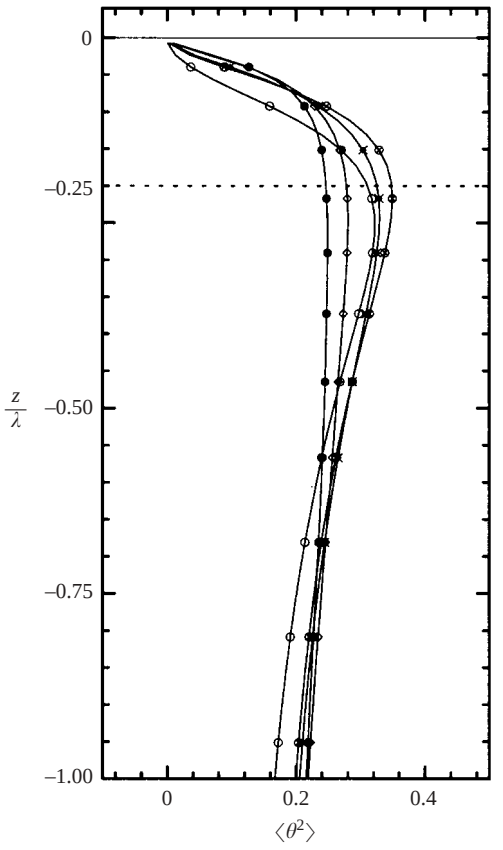

FIGURE 13. Vertical profiles of the scalar variance normalized by $(\Delta\theta)^2$ near the water surface. The dotted line is the breaker penetration depth. The different simulations are: ○, Couette; ⊗, $\mathscr{B}$-000; ⋆, $\mathscr{B}$-028; ◇, $\mathscr{B}$-080; ●, $\mathscr{B}$-100.

The spectra do not scale with u_* and z in the same way as separated flow over stationary roughness (e.g. Raupach *et al.* 1991). This is probably a consequence of the dynamic and intermittent nature of the breakers and the proximity of the location to the water surface. We show spectra near $z^+ = 15$, that is in the transition zone to the logarithmic region.

Previous flow visualization (§ 6.3) shows that breaking modifies the magnitude and distribution of instantaneous momentum flux. Breaking's contribution to the mean balance of horizontal momentum is contained in the conservation rule

$$\langle\tau_b\rangle = \langle\tau(z)\rangle - \langle u'w(z)\rangle + \left\langle \int_{-H}^{z} A_o \,\mathrm{d}z \right\rangle - \frac{\partial}{\partial t}\int_{-H}^{z} \langle u\rangle \,\mathrm{d}z\,, \tag{6.3}$$

where the vertical integration of (4.1*a*) extends from the bottom of the computational domain ($z = -H$) to an arbitrary level z. The viscous stress $\tau(z) = Re^{-1}\partial u/\partial z$. In developing (6.3), we assume horizontal homogeneity and retain the time tendency of the bulk flow. For statistically steady flow with no breakers, (6.3) simply reduces to the statement that the total stress, i.e. the sum of the viscous and Reynolds stress, is constant with depth. In simulations with breaking however, we found that the time tendency (acceleration) of the bulk flow is small, but nevertheless contributes to the mean balance of momentum. Our estimate of this term is obtained by first

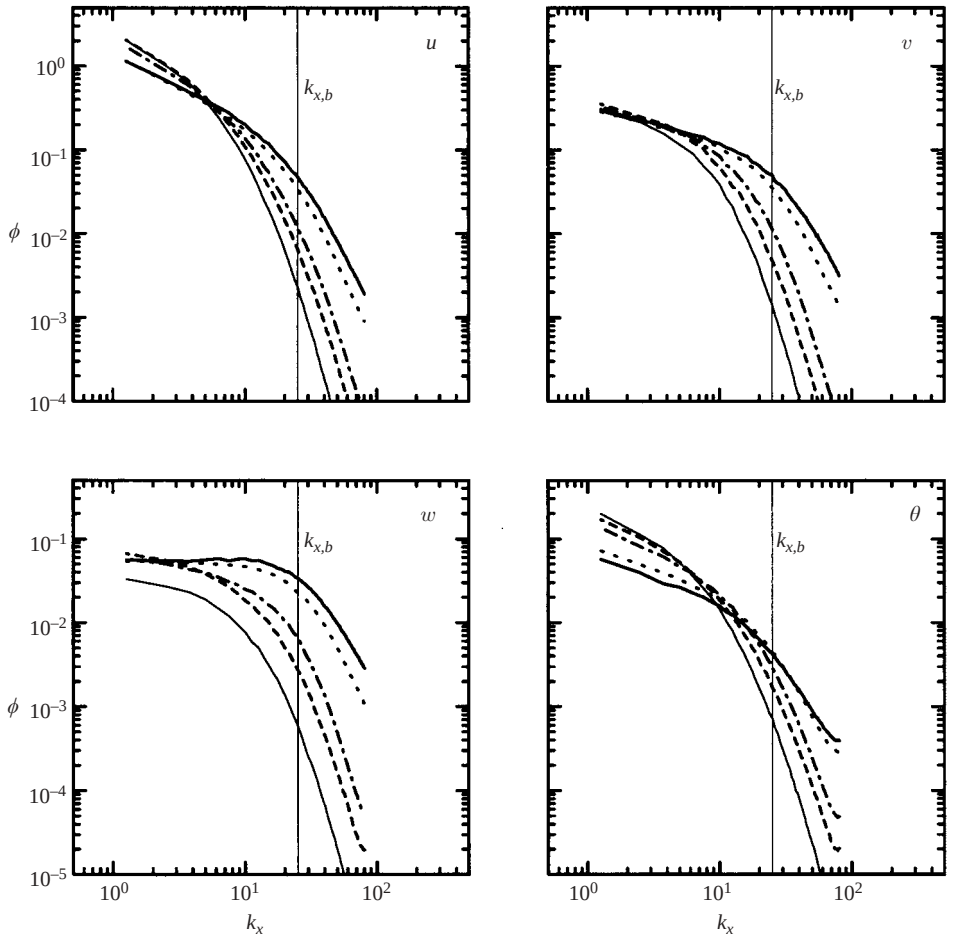

FIGURE 14. One-dimensional longitudinal spectra $\phi(k_x)$ of (u, v, w, θ) near the water surface, $z = -0.2\lambda$. Thick line, case $\mathscr{B}$-100; dotted line, $\mathscr{B}$-080; dash-dotted line, $\mathscr{B}$-028; dashed line, $\mathscr{B}$-000; and thin line, Couette. Velocity spectra are normalized by u_*^2 and the scalar spectra are normalized by θ_*^2. The thin vertical line is the wavenumber $k_{x,b} = 2\pi/\lambda$ of the imposed breakers.

computing $\int_{-H}^{z} \langle u \rangle_{xy} \, \mathrm{d}z$ at every time step and z of interest and then fitting a linear curve to the resulting time series. The slope serves as an estimate of the time-tendency contribution. Figure 15 shows the horizontal momentum budget for the different simulations. We observe that the contribution of all intermittent breaking events to the momentum budget decreases rapidly in the breaking region as $z/\lambda \to -0.2$. This is expected given our specified vertical shape function and $\chi = 0.2$. Meanwhile, the average Reynolds stress $\langle -u'w \rangle$ increases with the amount of breaking. This is consistent with the finding of Melville *et al.* (2002) that an isolated breaker generates a net $\langle u'w \rangle_{xy} < 0$. Since u_*^2 is nearly constant, the larger values of $\langle -u'w \rangle$ in the DNS are compensated by a reduction in the viscous stress. Compared to the Couette case, near-surface breaking influences the balance of turbulent and viscous stress to a depth of about $z/\lambda = -0.7$. The maximum contribution of the time dependence of the bulk flow is about 5% in the case with 100% breaking, and hence breakers lead to a weakly unsteady mean flow.

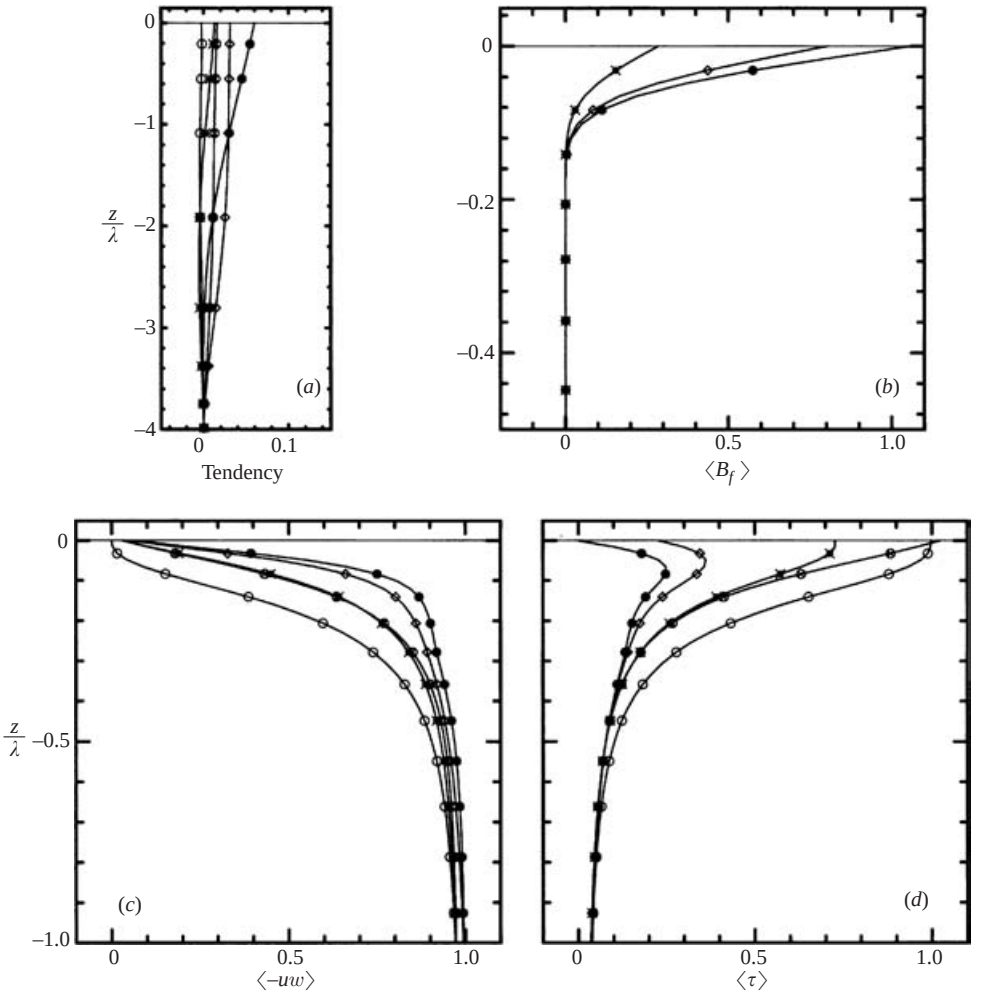

FIGURE 15. Terms in the horizontal mean momentum budget: (*a*) the time tendency of the bulk flow (see (6.3)); (*b*) the momentum flux from breakers, $\langle B_f \rangle = \langle \int_{-H}^{z} A_o \, \mathrm{d}z \rangle$; (*c*) the Reynolds stress $\langle -u'w \rangle$; and (*d*) the viscous stress $Re^{-1}\mathrm{d}\langle u \rangle/\mathrm{d}z$. All terms are normalized by the bottom stress $\langle \tau_b \rangle$. Note the different vertical scales used. The different simulations are: ○, Couette; ⊗, $\mathscr{B}$-000; ⋆, $\mathscr{B}$-028; ◇, $\mathscr{B}$-080; ●, $\mathscr{B}$-100.

6.6. *Eddy viscosity and TKE budget*

A cornerstone of most ensemble-closure modelling is the assumption of an eddy viscosity relationship between the vertical momentum flux and the mean profile gradient. In figure 16, we show estimates of the eddy viscosity K_m obtained from $\langle u'w \rangle = -K_m \mathrm{d}\langle u \rangle/\mathrm{d}z$ for the different simulations. Compared to the Couette case, K_m is enhanced by breaking down to a depth of about $z/\lambda \approx -0.5$; K_m is a factor of (4, 12.7) times larger at $z/\lambda = -(0.2, 0.1)$. This increase in eddy viscosity is a reflection of the reduction in the mean profile gradient and larger (more negative values of) Reynolds stress. Hence, in the OBL the surface-layer ensemble eddy viscosity depends on the magnitude and intermittency of breaking and is not equivalent to its atmospheric counterpart developed for flow over a passive rough wall. A similar variation in the mean eddy diffusion for a scalar is also found.

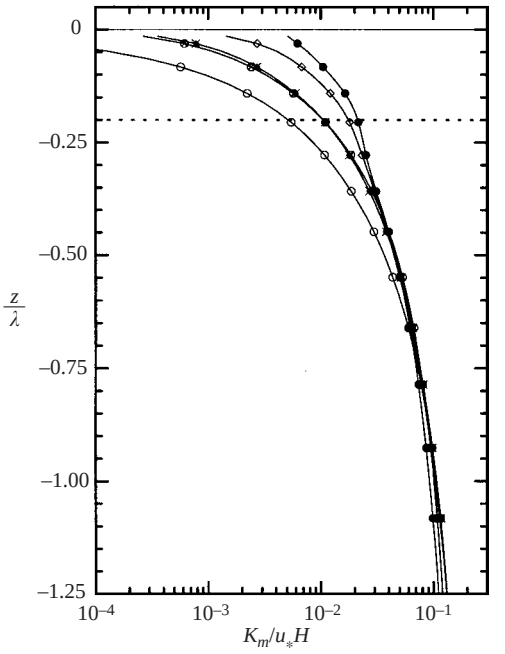

FIGURE 16. Vertical profiles of the momentum eddy diffusivity computed from $\langle u'w\rangle = -K_m \mathrm{d}\langle u\rangle/\mathrm{d}z$ near the water surface. The dotted line is the maximum breaker penetration depth. The different simulations are: ○, Couette; ⊗, $\mathscr{B}$-000; ⋆, $\mathscr{B}$-028; ◇, $\mathscr{B}$-080; ●, $\mathscr{B}$-100.

The turbulent kinetic energy (TKE) budget provides additional insight into how breaking couples to the turbulence fields. Under the assumption of a statistically steady flow, the budget for the TKE $q^2/2 = u_i'u_i'/2$ is

$$0 \approx \underbrace{-\frac{\mathrm{d}}{\mathrm{d}z}\frac{\langle wq^2\rangle}{2}}_{T_t} \underbrace{-\frac{\mathrm{d}}{\mathrm{d}z}\langle wp'\rangle}_{P_t} + \underbrace{\frac{1}{Re}\frac{\mathrm{d}^2}{\mathrm{d}z^2}\frac{\langle q^2\rangle}{2}}_{V_d} \underbrace{-\langle u'w\rangle\frac{\mathrm{d}\langle u\rangle}{\mathrm{d}z}}_{Prod} \underbrace{-\frac{1}{Re}\left\langle \frac{\partial u_i'}{\partial x_j}\frac{\partial u_i'}{\partial x_j}\right\rangle}_{\epsilon} + \underbrace{\langle A_o u'\rangle}_{B_w} \tag{6.4}$$

where terms on the right-hand side are the usual ones: turbulent transport of kinetic energy, pressure transport, viscous diffusion, production, and viscous dissipation. $\langle A_o u'\rangle$ is the new breaker work term. In the above budget, the time tendency of TKE is zero for simulations with constant-stress or -current boundary conditions and no breaking. However, similar to the budget of horizontal mean momentum, the time tendency of q^2 is small but finite near the water surface in the case with 100% breaking; $\partial\langle q^2/2\rangle/\partial t$ contributes about 6% to the budget. For clarity, we do not present the vertical profile of this term.

In figure 17, we show the different terms in the budget for the Couette, $\mathscr{B}$-000, and $\mathscr{B}$-100 simulations over the depth from $z/\lambda = -1$ to 0. The vertical profiles of the various terms in the Couette case agree quite well with other DNS (e.g. Papavassiliou & Hanratty 1997); near the upper surface the budget is primarily a balance between viscous dissipation and production with small contributions from the viscous diffusion and turbulent transport terms. In the τ-driven flow (no breakers) the balance of terms is similar with even smaller contributions from turbulent transport and viscous diffusion.

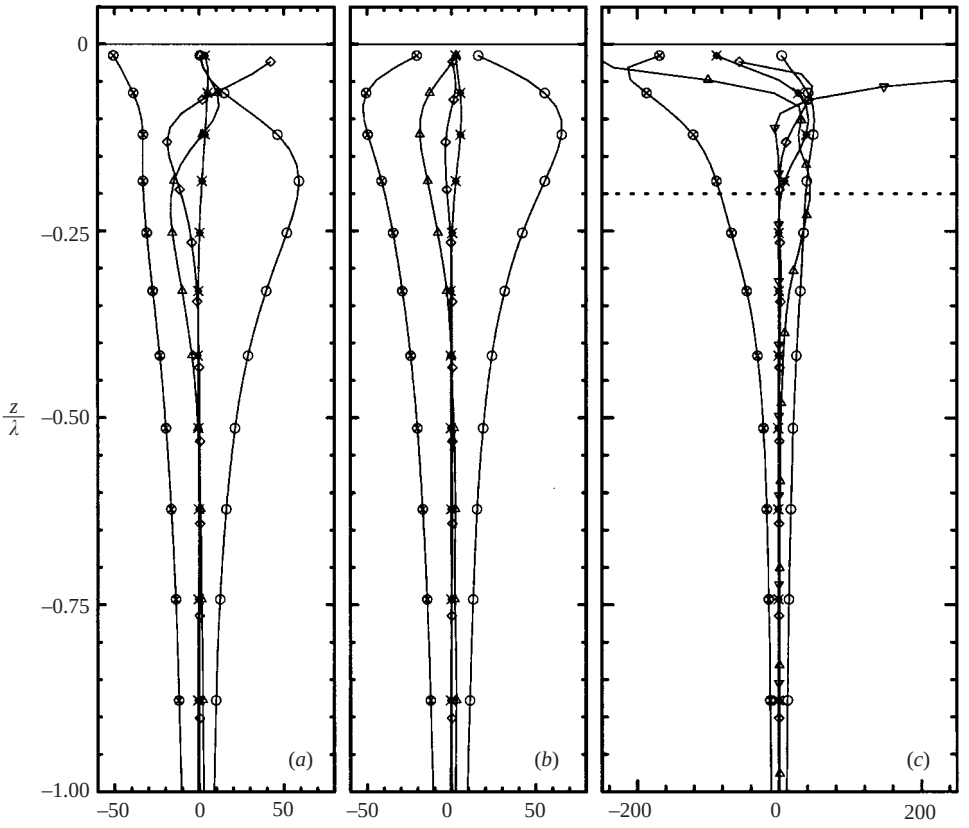

FIGURE 17. Vertical profiles of the terms in the turbulent kinetic energy (TKE) budget (see (6.4)) for three different cases: (*a*) Couette flow, (*b*), τ-driven flow with no breakers ($\mathscr{B}$-000), and (*c*) τ-driven flow with 100% breaking ($\mathscr{B}$-100). Lines with symbols denote terms in the TKE budget: ○, shear production; ⊗, viscous dissipation; ⋆, pressure transport; ◇, viscous diffusion; Δ, turbulent transport; and ▽, breaker work. For case $\mathscr{B}$-100 the breaker depth is denoted by a dotted line and the scale of the x-axis is wider. All terms are normalized by u_*^3/H.

In case $\mathscr{B}$-100, breaking waves are observed to alter the magnitude and sign of several terms in the TKE budget and as a result the usual balance of production $\approx$ dissipation for a shear flow is disrupted in the near-surface region. As expected, the primary source of TKE near the water surface is breaker work (figure 17*c*), and the turbulence dynamics respond by increasing the dissipation and enhancing the turbulent transport. Note that individually the magnitudes of T_t and B_w can exceed ϵ. In the breaking region, turbulent transport is a significant contributor to the TKE budget, in contrast to the no breaker cases where T_t is small for all z. Notice that at the maximum depth of penetration of the breakers ($z/\lambda = -0.2$), T_t is a source of TKE and is of comparable magnitude to the shear production; these two terms approximately balance the dissipation at this depth. Yet, the variation of T_t is complex as it switches sign as $z \to 0$ and becomes a significant TKE sink helping to balance the breaker work as shown in figure 18. Close to the water surface (figure 18) the sum $Prod + T_t + P_t + \epsilon + V_d$ serves as a sink to balance B_w. It is interesting to compare the present results with the assumptions made in the second-order closure models of Craig & Banner (1994) and Craig (1996). In these models,

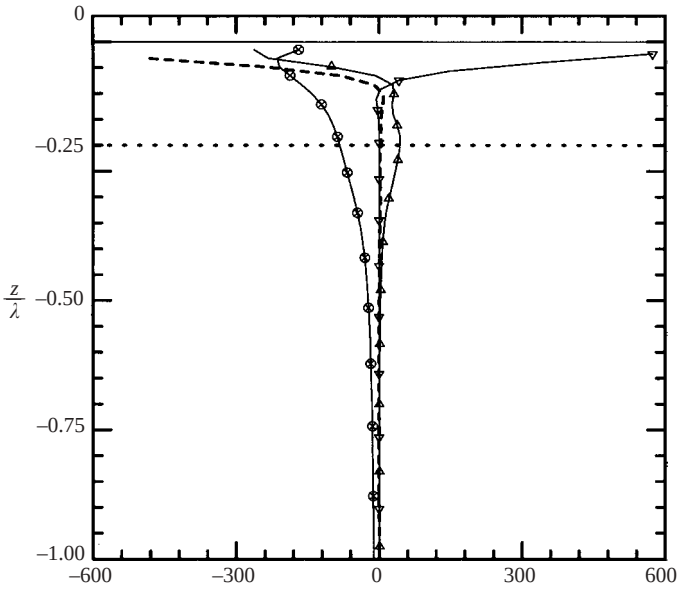

FIGURE 18. Vertical profiles of selected terms in the TKE budget for the simulations with 100% breaking. Lines with symbols denote the following terms: ⊗, viscous dissipation; Δ, turbulent transport; and ▽, breaker work. The sum $T_t + P_t + V_d + Prod + \epsilon$, indicated by a heavy dashed line, balances the breaker work very near the water surface. All terms are normalized by u_*^3/H.

the vertically distributed effects of breaking are compressed into a surface boundary condition. TKE is injected into the water column at $z = 0$ and diffuses vertically by the assumption of a downgradient model for the turbulent transport, i.e. $T_t \approx \epsilon$. Our computed budgets confirm that T_t is an important component in the TKE balance in the presence of breaking and that it can be a source of TKE for $z/\lambda < -0.2$. Yet, our TKE budget is a complex balance of terms in the breaking region, and these results do not support the assumption $T_t \approx \epsilon$ as in the second-order closure models (figures 17*c* and 18).

7. Conclusions

In this study, we used laboratory and field data to guide the development of a stochastic model of the effects of breaking surface gravity waves on the oceanic boundary layer. The parameterized breakers are 3D, time-dependent, and randomly distributed at the surface of the water. Critical constants in the breaker parameterization are the breaker strength and depth penetration length. This model is implemented in direct numerical simulations and evaluated in two classes of canonical flows: still fluid driven by an isolated breaker and idealized oceanic boundary layers with variable surface forcing.

We find that the single-breaker model is reasonably robust to changes in its parameterizations and is able to reproduce bulk features of an isolated breaking event. The decay of the mean-flow kinetic energy, the spatial and temporal flow patterns, and the formation of a coherent vortex beneath the water surface all agree reasonably well with laboratory data. Remnants of this vortex persist for at least 50 wave periods.

Highly intermittent active breaking (less than 2% of the water surface) has a significant impact on the near-surface currents in simulations of oceanic boundary layers. A vigorous, coherent, downwelling–upwelling pattern develops with each breaking event, and the lifetime of this flow structure is tens of wave periods. Breaking is found to induce high levels of turbulence, increase mixing, and promote vertical momentum transport near the water surface. Increased vertical velocity variances are observed down to a depth of $z/\lambda = -0.6$, where λ is the wavelength of the breaking wave. The effects of wave breaking are also readily visible in vertical profiles of the mean horizontal current. Compared to simulations driven by uniform stress, the current profiles with breaking show a large increase in surface roughness z_o; with 100% breaking z_o is 30 times larger and scaled by the breaker wavelength $z_o/\lambda \approx 0.05$. The budget of turbulent kinetic energy in the region of breaking waves is dominated by turbulent transport, dissipation, and breaker work, but the shear production, pressure transport and viscous diffusion remain non-negligible. At the maximum depth of penetration of breaking waves, turbulent transport is a source of turbulent kinetic energy and of comparable magnitude to the shear production. As $z \to 0$, turbulent transport switches sign, and breaker work is balanced by the sum of shear production, pressure and turbulent transports, viscous diffusion, and dissipation.

P. P. S. was partially supported by the Office of Naval Research through the CBLAST initiative, contract N00014-00-C-0180. W. K. M. was supported by grants from ONR (CBLAST) and the NSF (Physical Oceanography). NCAR is sponsored by the National Science Foundation.

REFERENCES

Adrian, R. J., Meinhart, C. D. & Tomkins, C. D. 2000 Vortex organization in the outer region of the turbulent boundary layer. *J. Fluid Mech.* **422**, 1–54.

Agrawal, Y. C., Terray, E. A., Donelan, M. A., Hwang, P. A., Williams 3rd, A. J., Drennan, W. M., Kahma, K. K. & Kitaigorodskii, S. A. 1992 Enhanced dissipation of kinetic energy beneath surface waves. *Nature* **359**, 219–220.

Anis, A. & Moum, J. N. 1995 Surface wave-turbulence interactions: Scaling $\epsilon(z)$ near the sea surface. *J. Phys. Oceanogr.* **25**, 2025–2045.

Banner, M. L., Jones, I. & Trinder, J. C. 1989 Wavenumber spectra of short gravity waves. *J. Fluid Mech.* **25**, 321–344.

Burchard, H. 2001 Simulating the wave-enhanced layer under breaking surface waves with two-equaiton turbulence models. *J. Phys. Oceanogr.* **31**, 3133–3145.

Cebeci, T. & Bradshaw, P. 1988 *Physical and Computational Aspects of Convective Heat Transfer*. Springer.

Chasnov, J. R. 1987 Simulation of the Kolmogorov inertial subrange using an improved subgrid model. *Phys. Fluids* A **3**, 188–200.

Chen, G., Kharif, C., Zaleski, S. & Li, J. 1999 Two-dimensional Navier-Stokes simulation of breaking waves. *Phys. Fluids* A **194**, 121–133.

Cheung, T. K. & Street, R. L. 1988 Turbulent layers in the water at an air-water interface. *J. Fluid Mech.* **194**, 133–151.

Craig, P. D. 1996 Velocity profiles and surface roughness under breaking waves. *J. Geophys. Res.* **101**, 1265–1277.

Craig, P. D. & Banner, M. L. 1994 Modeling wave-enhanced turbulence in the ocean surface layer. *J. Phys. Oceanogr.* **24**, 2546–2559.

Craik, A. & Leibovich, S. 1976 A rational model for Langmuir circulations. *J. Fluid Mech.* **73**, 401–426.

Dimas, A. & Fialkowski, L. T. 2000 Large-wave simulation (LWS) of free-surface flows developing weak spilling breaking waves. *J. Comput. Phys.* **159**, 172–196.

Donelan, M. A. 1998 Air-water exchange processes. In *Physical Processes in Lakes and Oceans*, *Coastal and Estuarine Studies*, vol. 54, pp. 19–36. American Geophysical Union.

Gemmrich, J. R. & Farmer, D. M. 1999 Near-surface turbulence and thermal structure in a wind-driven sea. *J. Phys. Oceanogr.* **29**, 480–499.

Kawamura, T. 2000 Numerical investigation of turbulence near a sheared air-water interface. Part 2: Interaction of turbulent shear flow with surface waves. *J. Mar. Sci. Tech.* **5**, 161–175.

Komminaho, J., Lundbladh, A. & Johansson, A. V. 1996 Very large structures in plane turbulent Couette flow. *J. Fluid Mech.* **320**, 259–285.

Lamarre, E. & Melville, W. K. 1992 Air entrainment and dissipation in breaking waves. *Nature* **351**, 469–472.

Large, W. G., McWilliams, J. C. & Doney, S. C. 1995 Oceanic vertical mixing: A review and a model with a nonlocal boundary layer parameterization. *Rev. Geophys.* **32**, 363–403.

Large, W. G. & Pond, S. 1982 Sensible and latent heat flux measurements over the ocean. *J. Phys. Oceanogr.* **12**, 464–484.

Leith, C. 1990 Stochastic backscatter in a subgrid-scale model: Plane shear mixing layer. *Phys. Fluids* **2**, 297–299.

Leonardi, S., Orlandi, P., Smalley, R. J., Djenidi, L. & Antonia, R. A. 2003 Direct numerical simulations of turbulent channel flow with transverse square bars on one wall. *J. Fluid Mech.* **491**, 229–238.

Loewen, M. R. & Melville, W. K. 1990 Microwave backscatter and acoustic radiation from breaking waves. *J. Fluid Mech.* **2**, 297–299.

Ly, L. & Garwood, R. W. 2000 Numerical modeling of wave-enhanced turbulence in the oceanic upper layer. *J. Phys. Oceanogr.* **56**, 373–383.

Mason, P. J. & Thomson, D. J. 1992 Stochastic backscatter in large-eddy simulations of boundary layers. *J. Fluid Mech.* **242**, 51–78.

McWilliams, J. C. 1996 Modeling the oceanic general circulation. *Annu. Rev. Fluid Mech.* **28**, 215–248.

McWilliams, J. C., Gallacher, P. C., Moeng, C.-H. & Wyngaard, J. C. 1993 Modeling the oceanic planetary boundary layer. In *Large-Eddy Simulations of Complex Engineering and Geophysical Flows* (ed. B. Galperin & S. A. Orszag), pp. 441–454. Cambridge University Press.

McWilliams, J. C. & Restrepo, J. M. 1999 The wave-driven ocean circulation. *J. Phys. Oceanogr.* **29**, 2523–2540.

McWilliams, J. C., Restrepo, J. R. & Lane, E. 2003 An asymptotic theory for the interaction of waves and currents in shallow coastal water. *J. Fluid Mech.* (submitted).

McWilliams, J. C. & Sullivan, P. P. 2001 Surface-wave effects on marine boundary layers. In *Fluid Mechanics and the Environment: Dynamical Approaches* (ed. J. Lumley), pp. 225–237. Springer-Verlag.

McWilliams, J. C., Sullivan, P. P. & Moeng, C.-H. 1997 Langmuir turbulence in the ocean. *J. Fluid Mech.* **334**, 1–30.

Melville, W. K. 1996 The role of wave breaking in air-sea interaction. *Annu. Rev. Fluid Mech.* **28**, 279–321.

Melville, W. K. & Matusov, P. 2002 Distribution of breaking waves at the ocean surface. *Nature* **417**, 58–63.

Melville, W. K., Veron, F. & White, C. J. 2002 The velocity field under breaking waves: coherent structures and turbulence. *J. Fluid Mech.* **454**, 203–233.

Moin, P. & Mahesh, K. 1998 Direct numerical simulation: A tool in turbulence research. *Ann. Rev. Fluid Mech.* **30**, 539–578.

Monahan, E. C. & Woolf, D. K. 1988 Comments on "Variations of whitecap coverage with wind stress and water temperature". *J. Phys. Oceanogr.* **19**, 706–709.

Papavassiliou, D. V. & Hanratty, T. J. 1997 Interpretation of large-scale structures observed in a turbulent plane Couette flow. *Intl J. Heat Fluid Flow* **18**, 55–69.

Phillips, O. M. 1985 Spectral and statistical properties of the equilbrium range in wind-generated gravity waves. *J. Fluid Mech.* **156**, 505–531.

Phillips, O. M. & Banner, M. L. 1974 Wave breaking in the presence of wind drift and swell. *J. Fluid Mech.* **66**, 625–640.

Phillips, O. M., Posner, F. L. & Hansen, J. P. 2001 High range resolution radar measurements of the speed distribution of breaking events in wind-generated ocean waves: Surface impulse and wave energy dissipation rates. *J. Phys. Oceanogr.* **31**, 450–460.

Rapp, R. J. & Melville, W. K. 1990 Laboratory measurements of deep-water breaking waves. *Phil. Trans. R. Soc. Lond.* A **331**, 735–800.

Raupach, M. R., Antonia, R. A. & Rajagopalan, S. 1991 Rough-wall turbulent boundary layers. *Appl. Mech. Rev.* **44**, 1–25.

Rhie, C. M. & Chow, W. L. 1983 A numerical study of the turbulent flow past an isolated airfoil with trailing edge separation. *AIAA J.* **21**, 1525–1532.

Robinson, S. K. 1991 Coherent motions in the turbulent boundary layer. *Annu. Rev. Fluid Mech.* **23**, 601–639.

Schlichting, H. 1968 *Boundary-Layer Theory*, 6th edn. McGraw-Hill.

Schumann, U. 1995 Stochastic backscatter of turbulence energy and scalar variance by random subgrid-scale fluxes. *Proc. R. Soc. Lond.* A **451**, 293–318.

Skyllingstad, E. D. & Denbo, D. W. 1995 An ocean large-eddy simulation of Langmuir circulations and convection in the surface mixed layer. *J. Geophys. Res.* **100**, 8501–8522.

Stacey, M. W. 1999 Simulation of the wind-forced near-surface circulation in Kinght inlet: A parameterization of the roughness length. *J. Phys. Oceanogr.* **29**, 1363–1367.

Sullivan, P. P. & McWilliams, J. C. 2002 Turbulent flow over water waves in the presence of stratification. *Phys. Fluids* **14**, 1182–1195.

Sullivan, P. P., McWilliams, J. C. & Moeng, C.-H. 1996 A grid nesting method for large-eddy simulation of planetary boundary layer flows. *Boundary-Layer Met.* **80**, 167–202.

Sullivan, P. P., McWilliams, J. C. & Moeng, C.-H. 2000 Simulation of turbulent flow over idealized water waves. *J. Fluid Mech.* **404**, 47–85.

Terray, E. A., Donelan, M. A., Agrawal, Y. C., Drennan, W. M., K. K. Kahma, A. J. W., Hwang, P. A. & Kitaigorodskii, S. A. 1996 Estimates of kinetic energy dissipation under breaking waves. *J. Phys. Oceanogr.* **26**, 792–807.

Thais, L. & Magnaudet, J. 1996 Turbulent structure beneath surface gravity waves sheared by the wind. *J. Fluid Mech.* **328**, 313–344.

Veron, F. & Melville, W. K. 2001 Experiments on the stability and transition of wind-driven water surfaces. *J. Fluid Mech.* **446**, 25–65.

Wu, J. 1988 Variations of whitecap coverage with wind stress and water temperature. *J. Phys. Oceanogr.* **18**, 1448–1453.

Zang, Y., Street, R. L. & Koseff, J. R. 1994 A non-staggered grid, fractional step method for time-dependent incompressible Navier-Stokes equations in curvilinear coordinates. *J. Comput. Phys.* **114**, 18–33.

Zhou, H. 1999 Numerical simulation of Langmuir circulations in a wavy domain and its comparison with the Craik-Leibovich theory. PhD thesis, Stanford University.